PHYSICAL REVIEW B **106**, 115430 (2022)

Stopping and image forces acting on a charged particle moving near a graphene-Al_2O_3-graphene heterostructure

Ana Kalinić,[1,2] Vito Despoja,[3,4,*] Ivan Radović,[2] Lazar Karbunar,[5] and Zoran L. Mišković[6]
[1]*School of Electrical Engineering, University of Belgrade, Bulevar Kralja Aleksandra 73, 11120 Belgrade, Serbia*
[2]*Department of Atomic Physics, VINČA Institute of Nuclear Sciences - National Institute of the Republic of Serbia, University of Belgrade, P.O. Box 522, 11001 Belgrade, Serbia*
[3]*Institute of Physics, Bijenička 46, 10000 Zagreb, Croatia*
[4]*Donostia International Physics Center (DIPC), P. Manuel de Lardizabal, 4, 20018 San Sebastián, Spain*
[5]*School of Computing, Union University, Knez Mihailova 6, 11000 Belgrade, Serbia*
[6]*Department of Applied Mathematics, and Waterloo Institute for Nanotechnology, University of Waterloo, Waterloo, Ontario, Canada N2L 3G1*

(Received 30 May 2022; revised 8 September 2022; accepted 13 September 2022; published 22 September 2022)

We study the impact of plasmon-phonon hybridization on the stopping and image forces acting on a charged particle moving parallel to a graphene-Al_2O_3-graphene sandwichlike composite system by considering a broad domain in the parameter space. The effective dielectric function of the system is obtained using two descriptions of the electronic response of doped graphene: an *ab initio* method based on the time-dependent density functional theory calculations and an analytical expression based on the massless Dirac fermion (MDF) approximation for graphene π bands. It is found that the main discrepancies between the two methods come from the high-energy interband electron transitions, which are included in the *ab initio* method but not in the MDF method. Special attention is paid to the regime of low-particle speeds, where the MDF method compares well with the *ab initio* method, but the modeling is sensitive to the effects of finite temperature and the treatment of phenomenological damping. It is observed at low particle speeds that both forces exhibit an interesting interplay between the hybrid modes of the phononic type and the continuum of the intraband electron-hole excitations in graphene. Furthermore, the effects of the lowest-energy antisymmetric modes, which exhibit acoustic dispersions at long wavelengths in a system with equally doped graphene layers, are exposed in calculations of the stopping force on a co-moving pair of incident particles with opposite charges that are symmetrically positioned around the target system.

DOI: 10.1103/PhysRevB.106.115430

I. INTRODUCTION

The discovery of graphene in 2004 by Novoselov and Geim [1] recommenced interest in the properties of two-dimensional (2D) electron systems. This monolayer of carbon atoms quickly became a very attractive material for numerous studies and also for potential technological applications [2]. The low-energy excitations in graphene may be described with its charge carriers treated as massless Dirac fermions (MDFs) [3,4]. Collective electron excitations, i.e., plasmon modes in graphene, are interesting from both experimental and theoretical points of view [5–15]. The three dominant types of electron excitations occurring in graphene include the DP (or sheet plasmon or 2D plasmon) and two spectrally significant features labeled as the π and $\sigma + \pi$ plasmons at ultraviolet frequencies. Dirac plasmon (DP) can only appear in doped graphene, as it represents charge density waves due to low-energy intraband excitations of charge carriers, and is active in the terahertz (THz) to the midinfrared (MIR) range of frequencies. On the other hand, π and $\sigma + \pi$ plasmons are high-energy interband transitions and can be found in doped and undoped graphene [16–18]. DP can be easily controlled by changing the doping density, thus enabling applications of graphene in photonics, optoelectronics, and plasmonics [19–22]. However, experimental designs of layered heterostructures involving graphene require stacking of graphene sheets with insulating spacer layers [23–25], which usually support strong Fuchs-Kliewer (FK) or optical surface phonon modes [26]. Those phonon modes are active in the same frequency range as the DP and can dampen it [27] or hybridize [28] with it. Such hybridization between plasmons and phonons can change the dispersion of the collective modes in supported graphene and, consequently, substantially affect its tunability for optoelectronics and plasmonics applications [29].

There has been a recent surge of interest in linearly dispersing polariton modes, with a special emphasis on the so-called acoustic plasmon (AP) in doped graphene because of its ability to compress optical fields to a nanometric space [30,31]. AP may be generated when a doped graphene sheet is placed in the proximity of a highly conductive metallic surface or when it lies parallel to a nearby 2D conductive layer [12,13,32]. In particular, a structure based on the spatially

---

[*] vdespoja@ifs.hr

separated double-layer graphene was predicted theoretically to give rise to two hybridized modes [33,34]: a higher-energy plasmon with a similar square-root dispersion as the DP of a single graphene sheet and a lower-energy, linearly dispersing AP [33,34]. An interesting application of such a structure was recently demonstrated in an experiment on molecular infrared spectroscopy employing a double-layer graphene AP resonator [35]. Although, while the linear dispersion of the AP in double-layer graphene is particularly appealing for nanophotonic and sensing applications, the presence of phonon modes in the dielectric spacer between the two graphene sheets gives rise to a strong plasmon-phonon hybridization, which may destroy the linear dispersion of the AP in the long wavelength limit [36].

The interaction of moving electrons or ions with the mentioned heterostructures can be used for probing plasmon-phonon hybridization, namely, a charged particle traveling parallel to a metallic or polar crystal surface induces excitations of single electrons and collective modes in that surface. The onset of the collective oscillations in the polarization of the medium is characterized by an oscillatory potential known as the wake effect. This effect arises in the induced electrostatic potential when the speed of the incident particle matches the phase velocity of collective oscillations [37,38]. The wake effect in a 2D conductive material was investigated theoretically in a strongly coupled 2D electron gas [39], followed by several studies in carbon nanostructures, including graphene [40–49]. Dynamic polarization of graphene also affects charged particles moving parallel to it; specifically, it has an impact on the stopping force and the image force. The stopping force represents the rate of dissipation of the particle's kinetic energy into plasmon excitations in graphene, and the image force describes the conservative force attracting the charge particle toward graphene. These forces were previously investigated in various systems involving graphene [29,41,42,47–60], e.g., with graphene supported by a SiO_2 or SiC substrate. In this paper, we shall explore the impact of plasmon-phonon hybridization on the stopping and image forces acting on a point charge moving parallel to a graphene-Al_2O_3-graphene (for short, denoted by gr-Al_2O_3-gr) composite system.

In our previous publication [36], we found that a sandwich-like gr-Al_2O_3-gr structure supports a variety of interesting plasmon-phonon hybrid modes. A thin layer of Al_2O_3, which is an experimentally often used dielectric spacer [61–63], supports two prominent transverse optical (TO) phonon modes in its bulk. Thus, there are two strongly coupled pairs of the FK phonon modes that are localized at each surface of the Al_2O_3 layer. Combining these phonon modes with the DP-AP pair of modes originating from two doped graphene layers, one can observe up to six well-defined hybrid modes in the THz to MIR frequency range. In the case when the graphene layers are equally doped, the hybrid modes can be classified by their symmetry into three symmetric and three antisymmetric modes, which are characterized by the induced potential in the structure that are even and odd functions of the perpendicular coordinate, respectively. This analysis in Ref. [36] was accomplished by deriving an expression for the effective 2D dielectric function of the said system using two complementary methods for graphene's electronic response: one based on the MDF approximation and the other one was the *ab initio* approach. In Refs. [64,65], an expression for the total potential in the plane of the graphene layer closest to the incident particle was derived and the impact of plasmon-phonon hybridization on the wake effect was studied. Finally, general expressions for the stopping and image forces acting on the external charged particle moving parallel to the gr-Al_2O_3-gr composite system were obtained [66], which are the basis for this paper. In this paper, the impact of plasmon-phonon hybridization on the aforesaid forces is evaluated, including a comparison between the MDF and *ab initio* methods, by considering three different doping densities of graphene, two different thicknesses of the Al_2O_3 layer, and three incident particle's distances from the nearest graphene layer.

Besides the parallel incidence of a single charged particle upon a gr-Al_2O_3-gr sandwich structure, we shall also consider in this paper the case of *two particles* moving at equal speeds in the same direction, symmetrically placed on the opposite sides of this structure. By allowing those particles to have equal and opposite charges, we propose a setting where the stopping force on those charges can be tuned to selectively probe the symmetric or antisymmetric hybrid plasmon-phonon modes in the structure. While such a setting may be challenging to realize in typical particle scattering experiments, the conclusions of our calculations for two co-moving charges could be extrapolated to a system where two symmetrically placed layers, that can conduct electron and/or hole currents, can interrelate with the gr-Al_2O_3-gr sandwich structure in a manner that is sensitive to the symmetry of its various hybrid modes.

It is worth mentioning that interactions of fast charged particles with carbon nanostructures have been studied in the context of electron energy loss spectroscopy (EELS), typically using a scanning transmission electron microscope (STEM) [67–69]. Moreover, the above described scattering geometry, where an incident charged particle moves (almost) parallel to the surface, may be of interest, e.g., for possible experiments using grazing scattering of fast ions [70,71] or for the aloof trajectories of the electron beam used for vibrational and valence EELS of layered heterostructures within a STEM [72]. External charges moving at lower energies, as in the reflection electron energy loss spectroscopy (REELS), may efficiently probe both the substrate surface phonons and the low-frequency plasmon modes in a 2D electron gas [73–75]. It is notable that both REELS and low-energy ion grazing scattering (LEIGS) [76–79] use charged particles that move at velocities comparable to the graphene Fermi speed, and are therefore perfectly suited to probe the plasmon-phonon hybridization in supported graphene.

This paper is organized as follows: After outlining the theoretical approach in the following section, we present and discuss the comparison between the MDF and *ab initio* methods for the stopping force and image force for a range of the relevant parameters. Concluding remarks are given in the last section. Note that we use Gaussian electrostatic units, set $\hbar = 1$, and denote the charge of a proton by $e > 0$.

II. THEORETICAL FORMULATION

A Cartesian coordinate system with coordinates $\{\mathbf{R}, z\}$ is used, where $\mathbf{R} = \{x, y\}$ is a 2D position vector in the xy plane

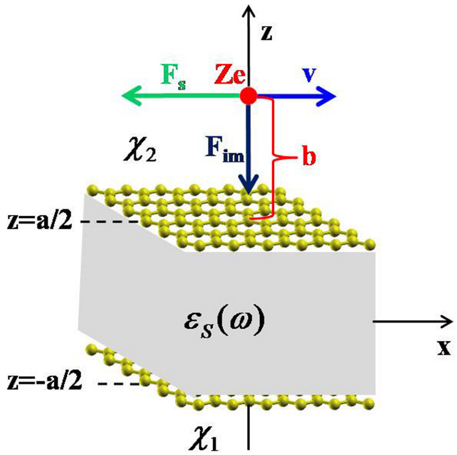

FIG. 1. Diagram of the stopping force F_s and the image force $F_{\rm im}$ that act on the point charge Ze moving parallel to the x axis with constant speed v at a fixed distance b above the gr-Al$_2$O$_3$-gr composite system. The polarization function of the top graphene layer placed in the $z = a/2$ plane is χ_2 and of the bottom in the $z = -a/2$ plane is χ_1. The Al$_2$O$_3$ layer of thickness a is described by local dielectric function $\epsilon_s(\omega)$.

and z is the distance from it. It is presumed that an incident particle with charge Ze and velocity $\mathbf{v}$ is moving parallel to a gr-Al$_2$O$_3$-gr composite structure at distance b from the top graphene surface, as depicted in Fig. 1. Assuming a translational invariance in the xy directions, a Fourier transform is performed, giving $\mathbf{R} \longmapsto \mathbf{Q}$. Two graphene layers occupy the $z = \pm a/2$ planes and there is no gap between them and the Al$_2$O$_3$ substrate. Bottom and top graphene sheets are described by the 2D response functions $\chi_1(Q, \omega)$ and $\chi_2(Q, \omega)$, respectively. It is assumed that each graphene layer is flat and isotropic and that no strain is applied to it. The Al$_2$O$_3$ layer is described by its local dielectric function $\epsilon_S(\omega)$. The entire system is assumed to be in vacuum or air.

A. Dynamic response functions of graphene layers

If the graphene layers are considered as strictly 2D systems, their nonlocal independent-electron response functions may be written as [80]

$$\mathcal{X}_i^0(\mathbf{Q}, z, z', \omega) = \chi_i^0(\mathbf{Q}, \omega)\delta(z - z_i)\delta(z' - z_i); \quad i = 1, 2, \tag{1}$$

where $\mathbf{Q}$ is the momentum transfer vector parallel to the (x, y) plane and $z_1 = -a/2$ and $z_2 = a/2$ are the locations of the layers on the z axis. The $\chi^0_{1,2}(\mathbf{Q}, \omega)$ functions are calculated from first principles as

$$\chi_i^0(\mathbf{Q}, \omega) = L\, \chi^{0,i}_{\mathbf{G}=0\mathbf{G}'=0}(\mathbf{Q}, \omega); \quad i = 1, 2, \tag{2}$$

where the 3D Fourier transform of the independent-electron response function is given by

$$\chi^{0,i}_{\mathbf{G}\mathbf{G}'}(\mathbf{Q}, \omega) = \frac{2}{\Omega}\sum_{\mathbf{K}\in \mathrm{SBZ}}\sum_{n,m} \frac{f_n^i(\mathbf{K}) - f_m^i(\mathbf{K}+\mathbf{Q})}{\omega + i\eta + E_n(\mathbf{K}) - E_m(\mathbf{K}+\mathbf{Q})} \times \rho_{n\mathbf{K},m\mathbf{K}+\mathbf{Q}}(\mathbf{G})\, \rho^*_{n\mathbf{K},m\mathbf{K}+\mathbf{Q}}(\mathbf{G}'); \quad i = 1, 2, \tag{3}$$

with $f^{1,2}_{n\mathbf{K}} = [e^{(E_{n\mathbf{K}} - E_F^{1,2})/kT} + 1]^{-1}$ being the Fermi-Dirac distributions at the temperature T. The charge vertices in Eq. (3) have the form

$$\rho_{n\mathbf{K},m\mathbf{K}+\mathbf{Q}}(\mathbf{G}) = \int_\Omega d\mathbf{r} e^{-i(\mathbf{Q}+\mathbf{G})\cdot\mathbf{r}}\, \phi^*_{n\mathbf{K}}(\mathbf{r})\phi_{n\mathbf{K}+\mathbf{Q}}(\mathbf{r}), \tag{4}$$

where $\mathbf{G} = (\mathbf{G}_\parallel, G_z)$ are the 3D reciprocal lattice vectors and $\mathbf{r} = (\mathbf{R}, z)$ is a 3D position vector. Integration in Eq. (4) is performed over the normalization volume $\Omega = S \times L$, where S is the normalization surface and L is superlattice constant in the z direction (separation between graphene layers in a superlattice arrangement). The plane-wave expansion of the wave function has the form

$$\phi_{n\mathbf{K}}(\mathbf{R}, z) = \frac{1}{\sqrt{\Omega}} e^{i\mathbf{K}\cdot\mathbf{R}} \sum_{\mathbf{G}} C_{n\mathbf{K}}(\mathbf{G}) e^{i\mathbf{G}\cdot\mathbf{r}},$$

where the coefficients $C_{n\mathbf{K}}$ are obtained by solving the local density approximation–Kohn Sham (LDA-KS) equations self-consistently.

B. The screened Coulomb interaction

If the geometry of the gr-Al$_2$O$_3$-gr composite is such that the Al$_2$O$_3$ slab occupies region $-a/2 < z < a/2$ and 2D graphene layers are laid in the planes $z = -a/2$ and $z = a/2$, then in the region $z > a/2$ and $z' > a/2$ the screened Coulomb interaction can be written as [36]

$$W(\mathbf{Q}, z, z', \omega) = v_Q e^{-Q|z-z'|} + W^{\rm ind}_{a/2,a/2}(\mathbf{Q}, \omega) e^{-Q(z+z'-a)}, \tag{5}$$

where

$$W^{\rm ind}_{a/2,a/2}(\mathbf{Q}, \omega) = \frac{v_{11} + v_{12}^2\chi_1 + v_{11}^2\chi_2 + v_{11}v_{12}^2\chi_1\chi_2}{1 - v_{12}^2\chi_1\chi_2} - v_Q \tag{6}$$

is a propagator of the induced Coulomb interaction at the surface $z = a/2$. Here, v_{11} and v_{12} represent propagators of bare Coulomb interaction within and between the surfaces $z = a/2$ and $z = -a/2$, respectively, screened by the dielectric Al$_2$O$_3$ slab, which have the following analytical form:

$$v_{11} = v_Q\left\{1 + D_S(\omega)\frac{1 - e^{-2Qa}}{1 - D_S^2(\omega)e^{-2Qa}}\right\}, \tag{7}$$

$$v_{12} = v_Q \frac{1 - D_S^2(\omega)}{1 - D_S^2(\omega)e^{-2Qa}} e^{-Qa}, \tag{8}$$

where $v_Q = 2\pi/Q$ and

$$D_S(\omega) = \frac{1 - \epsilon_S(\omega)}{1 + \epsilon_S(\omega)}.$$

Here, $\epsilon_S(\omega)$ represents the bulk dielectric function of Al$_2$O$_3$. The RPA screened response function of the ith graphene layer is

$$\chi_i(\mathbf{Q}, \omega) = \frac{\chi_i^0(\mathbf{Q}, \omega)}{1 - v_{11}(Q)\chi_i^0(\mathbf{Q}, \omega)}; \quad i = 1, 2. \tag{9}$$

Besides the one-sided screened Coulomb interaction, given in Eq. (6), we also require a two-sided interaction, enabling us to calculate stopping forces on two particles comoving on the opposite sides of the gr-$\mathrm{Al_2O_3}$-gr composite. In the regions $z > a/2$ and $z' < -a/2$, the screened Coulomb interaction can be written as [36]

$$W(\mathbf{Q}, z, z', \omega) = v_Q e^{-Q|z-z'|} + W^{\mathrm{ind}}_{a/2,-a/2}(\mathbf{Q}, \omega) e^{-Q(z-z'-a)}, \tag{10}$$

where

$$W^{\mathrm{ind}}_{a/2,-a/2}(\mathbf{Q}, \omega) = \frac{v_{12} + v_{11} v_{12}(\chi_1 + \chi_2) + v_{11}^2 v_{12} \chi_1 \chi_2}{1 - v_{12}^2 \chi_1 \chi_2} - v_Q e^{-Qa} \tag{11}$$

is the propagator of the induced Coulomb interaction between the surfaces $z = a/2$ and $z = -a/2$.

Finally, we note that removing the dielectric $\mathrm{Al_2O_3}$ slab leaves the formulas in Eqs. (5–11) unchanged, except that the intrasurface and intersurface Coulomb interactions in Eqs. (7) and (8) should be unscreened according to

$$v_{11} \rightarrow v_Q \tag{12}$$

and

$$v_{12} \rightarrow v_Q e^{-Qa}. \tag{13}$$

C. Stopping force and image force for one particle

Following the procedure outlined in the Supplemental Material (SM) [81], the stopping force on a charged particle Ze that moves in the x direction with constant speed v at a fixed distance b above the top graphene layer (so $z = a/2 + b$) is

$$F_s = \frac{(Ze)^2}{\pi^2} \int_0^\infty dQ_x \int_0^\infty dQ_y Q_x \times \mathrm{Im}[W(\mathbf{Q}, a/2 + b, a/2 + b, Q_x v)]. \tag{14}$$

Considering that $z, z' > a/2$, here we use the interaction Eq. (5) and obtain

$$\mathrm{Im}[W(\mathbf{Q}, a/2 + b, a/2 + b, Q_x v)] = e^{-2Qb} \mathrm{Im}\big[W^{\mathrm{ind}}_{a/2,a/2}(\mathbf{Q}, Q_x v)\big]. \tag{15}$$

Moreover, for one-sided interactions, we may also define an effective 2D dielectric function in terms of the screened Coulomb interaction at $z = z' = a/2$ as

$$\epsilon(\mathbf{Q}, \omega) = \frac{v_Q}{W(\mathbf{Q}, \frac{a}{2}, \frac{a}{2}, \omega)}. \tag{16}$$

After combining this with Eq. (15), we may write

$$\mathrm{Im}[W(\mathbf{Q}, a/2 + b, a/2 + b, Q_x v)] = v_Q e^{-2Qb} \mathrm{Im}\bigg[\frac{1}{\epsilon(\mathbf{Q}, \omega)}\bigg], \tag{17}$$

which, after inserting Eq. (17) back into Eq. (14), gives our final expression for the stopping force:

$$F_s = \frac{2(Ze)^2}{\pi} \int_0^\infty dQ_x \int_0^\infty dQ_y \frac{Q_x}{Q} e^{-2Qb} \mathrm{Im}\bigg[\frac{1}{\epsilon(\mathbf{Q}, Q_x v)}\bigg]. \tag{18}$$

After using Eqs. (5) and (6) in Eq. (16) and some algebra, the effective dielectric function may be written in a more explicit form as

$$\epsilon(\mathbf{Q}, \omega) = \frac{1}{2}\big[1 + \epsilon_S \coth(Qa) - 2 v_Q \chi_2^0\big] - \frac{1}{2} \frac{\epsilon_S^2 \,\mathrm{cosech}^2(Qa)}{1 + \epsilon_S \coth(Qa) - 2 v_Q \chi_1^0}. \tag{19}$$

Using similar argumentations and starting with the expression for the image force, derived in the SM,

$$F_{\mathrm{im}} = \frac{(Ze)^2}{\pi^2} \int_0^\infty dQ_x \int_0^\infty dQ_y \times \mathrm{Re} W_{\mathrm{ind}}(\mathbf{Q}, a/2 + b, a/2 + b, Q_x v), \tag{20}$$

where W_{ind} is obtained from Eq. (5) by removing the bare Coulomb interaction $v_Q e^{-Q|z-z'|}$, we can use the definition of the effective dielectric function in Eq. (16) to finally express the image force as

$$F_{\mathrm{im}} = \frac{2(Ze)^2}{\pi} \int_0^\infty dQ_x \int_0^\infty dQ_y e^{-2Qb} \mathrm{Re}\bigg[\frac{1}{\epsilon(\mathbf{Q}, Q_x v)} - 1\bigg]. \tag{21}$$

D. Stopping force for two particles

We now consider two charged particles, which move on the opposite sides of the gr-$\mathrm{Al_2O_3}$-gr composite with equal speeds, with their x coordinates both given by $x = vt$ and their z coordinates being $z = a/2 + b$ and $z = -a/2 - b$. We wish to evaluate the stopping force on one of the particles with charge Ze, moving at a distance b above the top graphene layer (so its z coordinate is $z = a/2 + b$) in the presence of another particle with the charge $\pm Ze$, moving at a distance b below the bottom graphene layer (so its z coordinate is $z = -a/2 - b$). Following the procedure outlined in the SM for the case of two particles, we obtain the stopping force on the first particle when the other particle is equally/oppositely charged as

$$F_s^{\pm} = \frac{(Ze)^2}{\pi^2} \int_0^\infty dQ_x \int_0^\infty dQ_y Q_x \times \{\mathrm{Im}[W(\mathbf{Q}, a/2 + b, a/2 + b, Q_x v)] \pm \mathrm{Im}[W(\mathbf{Q}, a/2 + b, -a/2 - b, Q_x v)]\}. \tag{22}$$

Here, we need the screened Coulomb interactions $W(\mathbf{Q}, z, z', \omega)$ for both one-sided cases with $z, z' > a/2$ and two-sided cases with $z > a/2$, $z' < -a/2$. After inserting the screened Coulomb interactions Eqs. (5) and (10), we obtain a more explicit expression:

$$F_s^{\pm} = \frac{(Ze)^2}{\pi^2} \int_0^\infty dQ_x \int_0^\infty dQ_y Q_x e^{-2Qb} \times \mathrm{Im}\big[W^{\mathrm{ind}}_{a/2,a/2}(\mathbf{Q}, Q_x v) \pm W^{\mathrm{ind}}_{a/2,-a/2}(\mathbf{Q}, Q_x v)\big]. \tag{23}$$

E. Computational details

The first part of our *ab initio* calculations consists of determining the KS ground state of single-layer graphene and the corresponding wave functions $\phi_{n\mathbf{K}}(\mathbf{R}, z)$ and energies $E_n(\mathbf{K})$. For graphene's unit-cell constant, we use the experimental value of $a_g = 0.245$ nm [82], while for the superlattice unit-cell constant (separation between the periodic replicas of graphene layers) we take $L = 5a_g$. For calculating the KS wave functions and energies, we use a plane-wave, self-consistent field code within density functional theory, within the QUANTUM ESPRESSO package [83]. The core-electron interaction is approximated by the norm-conserving pseudopotentials [84] and the exchange correlation potential by the Perdew-Zunger local density approximation [85]. To calculate the ground-state electronic density, we use $21 \times 21 \times 1$ Monkhorst-Pack K-point mesh [86] of the first Brillouin zone (BZ), and for the plane-wave cut-off energy we choose 50 Ry. The second part of our *ab initio* calculations consists of determining the independent-electron response function Eq. (3). To achieve better resolution in the long - wavelength limit ($Q \approx 0$) and the low-energy limit ($\omega \approx 0$), the response function Eqs. (3) and (4) is evaluated from the wave functions $\phi_{n\mathbf{K}}(\mathbf{r})$ and energies $E_n(\mathbf{K})$ calculated for the $601 \times 601 \times 1$ Monkhorst-Pack K-point mesh, which corresponds to 361 801 K points in the first BZ. The band summations (n, m) in Eq. (3) are performed over 30 bands. In the calculation, we use two kinds of damping parameters: $\eta_{\text{intra}} = 10$ meV for transitions within the same bands ($n \leftrightarrow n$) and $\eta_{\text{inter}} = 50$ meV for transitions between different bands ($n \leftrightarrow m$).

F. MDF model

The single-layer graphene response functions for noninteracting electrons were obtained at zero temperature using the random phase approximation (RPA) for doped graphene, taking into account just its π electron bands in the Dirac cone approximation [87,88] with the effects of damping included via the Mermin procedure for the damping parameter $\gamma = 10$ meV [60]. We call this approach the MDF method. This method accurately describes both the interband and the intraband electron transitions involving π electron bands at frequencies up to the IR for typical doping densities of graphene. It is assumed that graphene sheets are equally doped, each having the same Fermi energy, so the graphene layers have equal polarization functions, $\chi_1 = \chi_2$.

G. Al_2O_3 model dielectric function

The Al_2O_3 slab is treated as a homogeneous dielectric described by local dielectric function $\epsilon_S(\omega)$. Complex polar crystals, such as Al_2O_3, possess several different optical phonons with different symmetries and polarizations. But if we assume that the polarization of the bulk Al_2O_3 mainly comes from excitations of the two optical modes that have the largest oscillator strengths [26,89], its bulk dielectric function may be approximated by [90]

$$\epsilon_S(\omega) = \epsilon_{ox}^{\infty} + \left(\epsilon_{ox}^{i} - \epsilon_{ox}^{\infty}\right)\frac{\omega_{\text{TO2}}^2}{\omega_{\text{TO2}}^2 - \omega^2 - i\omega\gamma_{\text{TO2}}} + \left(\epsilon_{ox}^{0} - \epsilon_{ox}^{i}\right)\frac{\omega_{\text{TO1}}^2}{\omega_{\text{TO1}}^2 - \omega^2 - i\omega\gamma_{\text{TO1}}}, \qquad (24)$$

where ϵ_{ox}^{∞}, ϵ_{ox}^{i}, and ϵ_{ox}^{0} are the optical, intermediate, and static permittivities, ω_{TO1} and ω_{TO2} are the first and second TO angular frequencies (with $\omega_{\text{TO1}} < \omega_{\text{TO2}}$), and γ_{TO1} and γ_{TO2} are the damping rates of the corresponding TO phonons.

For the bulk Al_2O_3 dielectric function given in Eq. (24), we use the following parameters: $\epsilon_{ox}^{0} = 12.53$, $\epsilon_{ox}^{i} = 7.27$, $\epsilon_{ox}^{\infty} = 3.20$, $\omega_{\text{TO1}} = 48.18$ meV, $\omega_{\text{TO2}} = 71.41$ meV, $\gamma_{\text{TO1}} = 1.74$ meV and $\gamma_{\text{TO2}} = 6.82$ meV. After determining the response function in Eq. (3) and using the Al_2O_3 dielectric function in Eq. (24), the effective 2D dielectric function in Eq. (19) is calculated.

The thickness of the Al_2O_3 slab is a and, for simplicity, it is assumed that there is no gap between it and the two graphene layers. It was found that this approximation has negligible effects on the coupled modes. In our previous work [60], we studied the effects of this distance on the stopping and image forces in the case of graphene on a semi-infinite insulator and found that, while the zero-gap approximation yields qualitatively correct behavior of these forces, there are notable quantitative effects at the incident particle speeds $v \gtrsim v_F$, where $v_F \approx c/300$ is the Fermi speed of graphene's π electron bands and c is the speed of light in vacuum. Although the issue may be more complicated in the case of a sandwich structure with a relatively thin insulating layer, we believe that assigning a finite gap size in the present paper would not alter the results in a qualitative manner. A detailed study of the effects of finite gap is therefore deferred to future work.

III. RESULTS AND DISCUSSION

In our previous work, we found that, for a doped graphene sheet on a SiC [52] or a SiO_2 [29] substrate, there exists a velocity threshold at v_F, such that the excitation of the DP can occur if the charged particle moves at speeds $v > v_F$. Below the threshold, $v < v_F$, the stopping force showed a broad feature, which included a combination of contributions from the continuum of the intraband electron-hole (e-h) excitations in doped graphene and a low-frequency phonon mode in the case of a SiC substrate [52]. At the same time, the dynamic image force barely showed any effects of a SiO_2 substrate in the subthreshold range of speeds [29]. Our goal in this section is to explore the range of speeds up to $10\,v_F$, paying special attention to the subthreshold region, $v < v_F$, where we expect an evidence of the phonon excitation in both the stopping and image forces. These forces will be evaluated by using both MDF and *ab initio* methods for a particle moving parallel to the sandwichlike gr-Al_2O_3-gr composite shown in Fig. 1. We shall use the following set of parameters: three different doping densities of graphene (with $E_F = 0$ for undoped, and $E_F = 200$ meV or $E_F = 1000$ meV for doped graphene), two different thicknesses of the Al_2O_3 layer ($a = 5$ nm and $a \to \infty$ for semi-infinite dielectric), and three incident particle's distances from the nearest graphene layer ($b = 0.5$ nm, $b = 5$ nm, and $b = 50$ nm).

A. Stopping and image forces on single particle

First, let us explore in Fig. 2 the system consisting of two graphene sheets a distance $a = 5$ nm apart with the same doping density, which when expressed via its Fermi energy is given by $E_F = 200$ meV [marked as gr(200 meV)]. The region between the two graphene sheets is filled with either

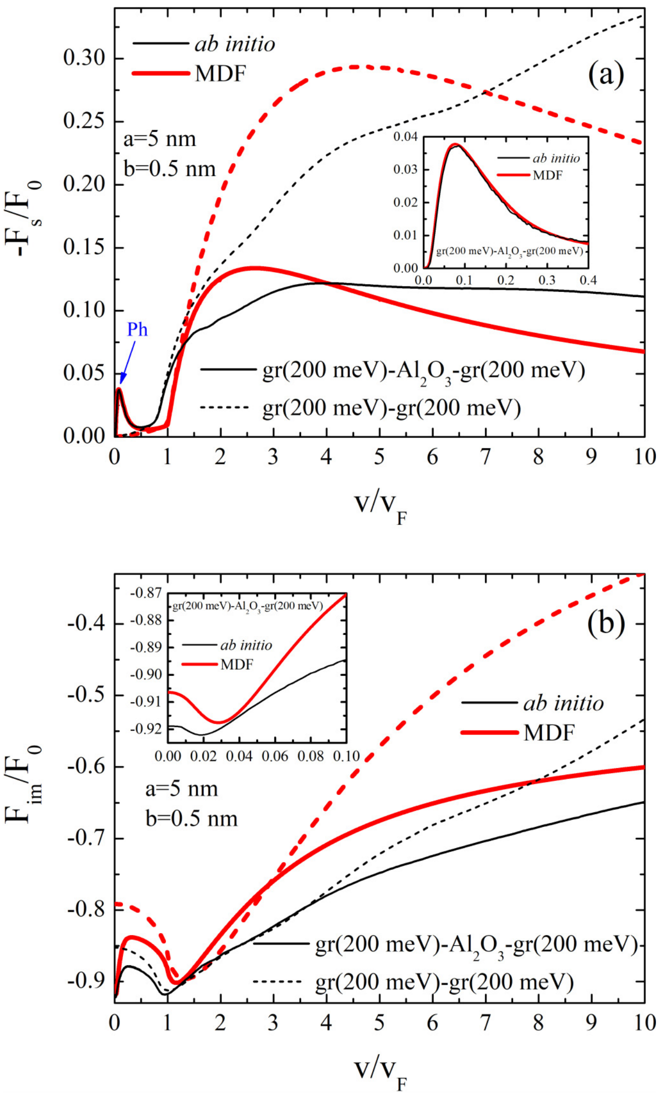

FIG. 2. The stopping force F_s (a) and the image force F_{im} (b), normalized by $F_0 = (Ze)^2/(4b^2)$, as functions of the speed v (normalized by v_F) of a charged particle ($Z = 1$) moving at a distance $b = 0.5$ nm above the top graphene. The separation between graphene layers (or the Al_2O_3 slab thickness) is $a = 5$ nm and both layers are doped such that $E_F = 200$ meV. Results are shown for two composite systems: gr-Al_2O_3-gr (solid lines) and gr-gr (short dashed lines). Thin black lines are obtained using the *ab initio* method and thick red lines using the MDF method. The insets show the zoom of panels (a) and (b) in the low-velocity regime in the case of the gr-Al_2O_3-gr composite.

an Al_2O_3 layer (solid lines) or air/vacuum (dashed lines). The distance from the charged particle to the top graphene layer is $b = 0.5$ nm. The stopping force acting on the charged particle traversing parallel to the described system is shown in Fig. 2(a), while the corresponding image force is shown in Fig. 2(b). We note that in Fig. S2 of the SM, we plotted the results for both forces on a gr-Al_2O_3-gr structure using the same distance $b = 0.5$ nm and the same doping $E_F = 200$ meV as in Fig. 2, but with the thickness increased to $a \to \infty$, and we found that they are practically identical with those obtained with $a = 5$ nm. This shows that, for the choice of parameters in Fig. 2, namely, $a \gg b$, the modes originating from the charge polarization on the opposing surfaces in a thick gr-Al_2O_3-gr structure are electrostatically decoupled, so the problem is reduced to that of a single sheet of doped graphene on a semi-infinite substrate, studied before [29,60].

In Fig. 2(a), the stopping force obtained with the MDF method exhibits a broad maximum, which occurs at about 2–3 v_F for the system with the Al_2O_3 layer and at about 4–5 v_F for the system without that layer, similar to the stopping force for single graphene sheet on a semi-infinite dielectric substrate [29,52]. As in those previous references, the broad maxima in Fig. 2(a) can be assigned to a high-energy, DP-like plasmonic hybrid mode, which follows a square-root dispersion (see Figs. 5 and 7 in Ref. [36] for the structure without and with the Al_2O_3 layer, respectively). On the other hand, the stopping force in Fig. 2(a) from the *ab initio* method levels off at an approximately constant value for $v \gtrsim 4\,v_F$, which is comparable to that attained at the peak in the MDF method for the system with Al_2O_3, while it continues to increase with the increasing speed in the range above v_F for the system without the Al_2O_3 layer. The differences between the MDF and the *ab initio* methods at high speeds may be explained by a contribution to the stopping force that comes from high-energy interband electron transitions in the *ab initio* method, which are not included in the MDF method. More specifically, with the contribution of the region with the $Q \gtrsim 1/(2b) = 1$ nm^{-1} values to the integrals defining the stopping and image forces being suppressed, the role of the high-energy interband transitions with energy, say, ω_{high} in the *ab initio* method can only be probed at high enough speeds, such that $v \gtrsim 2b\omega_{\mathrm{high}}$. Taking $\omega_{\mathrm{high}} = 4$ eV as a typical value corresponding to the π peak in graphene, we may estimate that significant deviations of the MDF method from the *ab initio* method would be expected at the speeds $v \gtrsim 6\,v_F$ for $b = 0.5$ nm.

In both the MDF and the *ab initio* methods, the stopping forces at speeds $v > v_F$ have significantly smaller magnitudes in the case with the Al_2O_3 than in the case without the Al_2O_3 layer, indicating a shift of the spectral weight toward the low-energy, phononlike hybridized modes [36]. This shift of weight in the presence of the Al_2O_3 layer will be a pervading qualitative observation in all the results on stopping force presented below, which will be rationalized in a more quantitative manner via the modal decomposition in Fig. 7. Here, in Fig. 2(a), we observe that the magnitudes of the stopping forces at low speeds, $v < v_F$, in the case without the Al_2O_3 layer are small in both methods and they only show a linear increase with the increasing speed due to the continuum of the intraband e-h excitations, corresponding to the regime of linear friction [52]. However, in the presence of the Al_2O_3 layer, both methods yield a stopping force that exhibits a sharp peak at the speed around $v = 0.08\,v_F$, as seen in the inset to Fig. 2(a). To elucidate the origin of that peak, let us derive approximate conditions on the charged particle's distance b and speed v, which will enable a low-energy, weakly dispersing optical phonon mode to make a sizable contribution to the stopping force. It is shown in Sec. S2.A of the SM that the location of the peak seen in the inset of Fig. 2(a) may be ascribed to a contribution coming from the FK phonon with the frequency $\omega_{\mathrm{FK2}} \approx 86$ meV, from the range of wave numbers outside the continuum of the intraband e-h excitations, where this mode is free from Landau damping. From Fig. S1(b), we can ascertain that this will be the case when $Q > 2k_F + \omega_{\mathrm{FK2}}/v_F$, where $k_F = E_F/v_F$ is the Fermi wave number in graphene. On the other hand, that FK mode can make a contribution to the stopping force if the resonance condition is fulfilled, $\omega_{\mathrm{FK2}} < Qv$. Moreover, keeping in mind that the effective range of the contributing wave numbers is bounded by $Q \lesssim 1/(2b)$, we may estimate that sizable effects of the FK phonon in the stopping force can be expected for short enough distances and the speeds, which satisfy the inequalities

$$\frac{1}{2b} \gtrsim \frac{\omega_{\mathrm{FK2}}}{v} \gtrsim 2k_F + \frac{\omega_{\mathrm{FK2}}}{v_F}, \tag{25}$$

giving the conditions $b \lesssim 0.7$ nm and $v \lesssim 0.2\, v_F$ for the doping of $E_F = 200$ meV. Clearly, the choice of $b = 0.5$ nm facilitates the appearance of a peak at $v \approx 0.08\, v_F$, whose width at half maximum satisfies the above condition on the particle speed, as evidenced in the inset to Fig. 2(a).

The inset in Fig. 2(a) also shows a remarkably close agreement between *ab initio* and MDF methods in the low-velocity range, from which we may conclude that the MDF method provides an adequate description of the fate of the substrate phonons, when they interact with the continuum of low-energy intraband e-h excitations at (relatively) large wave numbers.

In Fig. 2(b), the dependence of the image force on the speed in the case without the $\mathrm{Al_2O_3}$ layer resembles the typical results found previously for a single-layer free graphene, [29] exhibiting a local minimum near $v = v_F$, with a gradual approach to a constant value as $v \to 0$. The magnitude of the image force in the *ab initio* method is larger than that in the MDF method for speeds $v \gtrsim 2\, v_F$, with a difference that keeps growing with v, which is again likely related to contributions from the high-energy interband transitions that are included in the *ab initio* method. In the case with the $\mathrm{Al_2O_3}$ layer, the image forces obtained with the two methods are seen to be in closer agreement than in the case without that layer, and they both show a tendency to approach a value determined by a substrate with the dielectric constant ϵ_{ox}^{∞} as the speed increases [91]. Most strikingly, the two methods share interesting qualitative features in the dependence of the image force for the speed in the region $v < v_F$, where the stopping force was found to be dominated by the substrate FK phonon, namely, there is a local minimum in the inset to Fig. 2(b) for the image force at around $0.02\, v_F < v < 0.03\, v_F$, noticeable in both methods in the presence of the $\mathrm{Al_2O_3}$ layer, which is related to the local maximum seen in the inset to Fig. 2(a) for the stopping force at around $v = 0.08\, v_F$. This local minimum in the image force with the $\mathrm{Al_2O_3}$ layer is followed by a broad, asymmetric local maximum at $v \approx 0.25\, v_F$ in Fig. 2(b), which gradually evolves into another local minimum at about $v = v_F$ that apparently shares the same origin as the minimum observed in the case without the $\mathrm{Al_2O_3}$ layer.

The curves obtained from the MDF and *ab initio* methods for the image force at low speeds, $v < v_F$, look qualitatively similar, but they exhibit small vertical and horizontal shifts. This difference between the two methods may be attributed to the limit of static screening, where static in-plane polarizability of graphene can be strongly affected by the high-energy interband transitions in graphene [32,92], which are included in the *ab initio* method but are missing in the MDF method. Next, we increase the Fermi energy of the graphene sheets to $E_F = 1000$ meV. Figure 3 shows the stopping and image forces in the gr(200 meV)-$\mathrm{Al_2O_3}$-gr(200 meV) and gr(1000 meV)-$\mathrm{Al_2O_3}$-gr(1000 meV) systems. We see that, while the increase in the doping density in Fig. 3 has negligible effects on both forces at the speeds exceeding 3–4 v_F within both methods, there is a notable increase in the magnitudes of both forces at speeds $v_F \lesssim v \lesssim$ 3–4 v_F when going from $E_F = 200$ meV to $E_F = 1000$ meV. Given

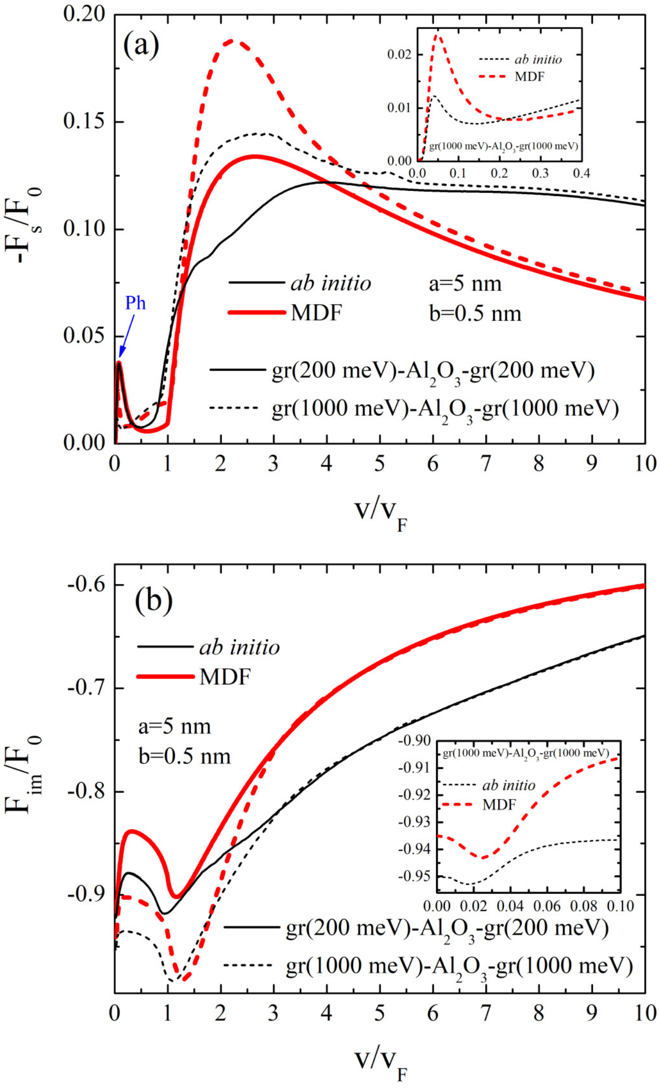

FIG. 3. The stopping force F_s (a) and the image force F_{im} (b), normalized by $F_0 = (Ze)^2/(4b^2)$, as functions of the speed v (normalized by v_F) of a charged particle moving at a distance $b = 0.5$ nm above the gr-$\mathrm{Al_2O_3}$-gr composite system. The thickness of the $\mathrm{Al_2O_3}$ layer is $a = 5$ nm. Results are shown for two values of the Fermi energies, same for both graphene layers: $E_F = 200$ meV (solid lines) and $E_F = 1000$ meV (short dashed lines). Thin black lines are obtained using the *ab initio* method and thick red lines using the MDF method. The insets show the zoom of panels (a) and (b) in the low-velocity regime when both graphene layers are doped such that $E_F = 1000$ meV.

that we may still expect that the two surfaces in our sandwich structure are electrostatically decoupled for the chosen a and b values in Fig. 3, this increase of magnitudes may be simply assigned to an increase of the energy of the DP-like hybrid mode due to an increase in the doping density of graphene, as previously observed for single layer graphene [29]. In the range of low speeds, $v < v_F$, we also see some quantitative changes in the contribution of the substrate phonons to the stopping force. Comparing the insets in Figs. 2(a) and 3(a), we see that the increase in the doping density reduces the magnitude of the phonon-induced peak in the stopping force and pushes it to a lower speed, $v \approx 0.04$–$0.05\ v_F$, followed by a broad minimum around $v = 0.1\,v_F$ for the *ab initio* method and around $v = 0.2\,v_F$ for the MDF method, giving rise to a small difference between the two methods, which was not seen in the inset to Fig. 2(a).

The changes in the low-velocity region of the stopping force can be analyzed in view of the conditions derived above, which now give $b \lesssim 0.15$ nm and $v \lesssim 0.04\,v_F$ for the doping of $E_F = 1000$ meV. These inequalities indicate that increasing the doping density in Fig. 3 is not favorable for the appearance of a signature of the FK phonon mode in the stopping force in the form of a sharp peak at $v \ll v_F$. While the phonon-induced peak is suppressed in the stopping force, we see that a region with linear increase of that force takes over as the speed increases beyond $v = 0.1\,v_F$ for the *ab initio* method and beyond $v = 0.2\,v_F$ for the MDF method, indicating the onset of the friction regime due to the intraband e-h excitations in graphene doped at $E_F = 1000$ meV.

Similar changes are visible in Fig. 3(b) for the image force, which exhibits an increase in the magnitude at speeds $v < 3\,v_F$ in both methods. A closer inspection of the low-velocity region in the inset to Fig. 3(b) also reveals some small changes in the shape of the image force curves in the two methods with the doping $E_F = 1000$ meV, with the minima still occurring at about the same speeds, $0.02\,v_F < v < 0.03\,v_F$, as in the case with the doping $E_F = 200$ meV, discussed in the inset to Fig. 2(b). In Fig. 4, we show the stopping force in the range of speeds from 0 to v_F for two undoped graphene sheets a distance $a = 5$ nm apart, with and without the Al_2O_3 layer, as well as for the sheets with the two doping densities from Fig. 3 with the Al_2O_3 layer, using the same particle distance $b = 0.5$ nm. It is seen that all the curves from the *ab initio* and the MDF methods agree reasonably well up to the speed $\sim 0.5\,v_F$, except for the undoped case without the Al_2O_3 layer. All the curves obtained from the *ab initio* method show a rapid increase in the stopping force at speeds $0.8\,v_F \lesssim v < v_F$, which is not evident in the curves from the MDF method. We recall that the speed $v = v_F$ corresponds to a threshold for excitations of the e-h continuum due to the interband transitions involving the π electron bands in graphene. Therefore, the discrepancy between the two methods in Fig. 4 when the speed approaches this value is likely due to the fact that the *ab initio* method uses a rather large damping rate of $\eta_{\text{inter}} = 50$ meV for the interband transitions, whereas the MDF method uses the damping of $\gamma = 10$ meV for both the intraband and interband transitions. This point is further analyzed in Fig. S3 of the SM.

In Sec. S2.A of the SM, we show that the peak at the speed $v \lesssim 0.08\,v_F$ is related to the FK phonon with higher frequency of the two FK phonons in a Al_2O_3 surface, $\omega_{\text{FK2}} = 86$ meV, which is modified by static screening in graphene. The peak region up to $\sim 0.2\,v_F$ in Fig. 4 is not affected by the method used nor by the change in the doping density from $E_F = 0$ to $E_F = 200$ meV, confirming the dominant role of that FK phonon mode in the Al_2O_3 layer. The curves with the doping increased to $E_F = 1000$ meV in Fig. 4 reveal additional details of the case discussed in the inset to Fig. 3(a), with the weight of the peak lowered and its position reduced to about 0.04–$0.05\ v_F$, accompanied by an onset of a quasi-linear increase of the stopping force in the range of speeds $0.2\,v_F \lesssim v \lesssim 0.8\,v_F$ for both methods. The differences seen in Fig. 4 between the curves obtained with the two methods at the doping $E_F = 1000$ meV, which include the peak heights and positions, as well as a small vertical shift of the stopping force in the linear region, may be related to the fact that the temperature was taken to be room temperature in the *ab initio* method, while the MDF method is formulated for zero temperature. However, it is more likely that the difference arises in the static screening of the substrate phonons by graphene due to different treatments of the damping factors, namely, the MDF method employs Mermin's procedure, while the *ab initio* method does not. The largest difference between the two methods is seen in Fig. 4 for the case of undoped graphene sheets without the Al_2O_3 layer, where a linear increase of the stopping force with increasing speed in the *ab initio* method occurs at a much higher rate than in the MDF method. This is likely to be due to the effects of both finite temperature and larger damping rate for the interband transitions in the

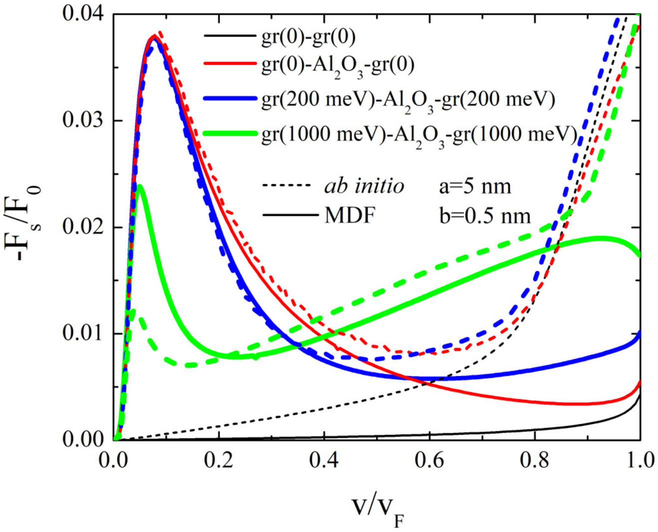

FIG. 4. The stopping force F_s normalized by $F_0 = (Ze)^2/(4b^2)$ as a function of the speed v (normalized by v_F) of a charged particle moving at a distance $b = 0.5$ nm above the top graphene. The separation between graphene layers is $a = 5$ nm. Results are shown for four composite systems: two undoped graphene layers (thin black lines), two undoped graphene layers with Al_2O_3 in between (medium red lines), two graphene sheets with Fermi energy of $E_F = 200$ meV with Al_2O_3 in between (thick blue lines), and the same system but with $E_F = 1000$ meV (extra thick green lines). Short dashed lines are obtained using the *ab initio* method and solid lines using the MDF method.

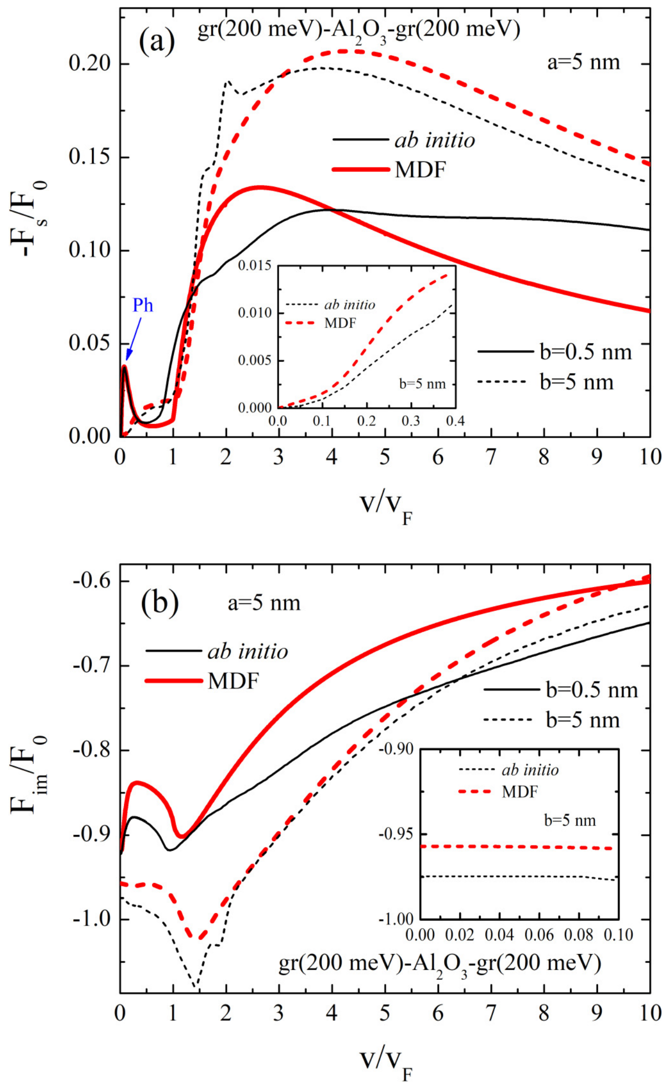

FIG. 5. The stopping force F_s (a) and the image force F_{im} (b), normalized by $F_0 = (Ze)^2/(4b^2)$, as functions of the speed v (normalized by v_F) of a charged particle moving at two distances above the gr-Al$_2$O$_3$-gr composite system: $b = 0.5$ nm (solid lines) and $b = 5$ nm (short dashed lines). The separation between graphene layers or the Al$_2$O$_3$ slab thickness is $a = 5$ nm and both layers are doped such that $E_F = 200$ meV. Thin black lines are obtained using the*ab initio* method and thick red lines using the MDF method. The insets show the zoom of panels (a) and (b) in the low-velocity regime for the charged particle distance of $b = 5$ nm.

ab initio method. In any case, based on the above discussion of Fig. 4, as well as in the discussion of Fig. S3 in the SM, we may conclude that modeling of the substrate phonon influence on the stopping force at low speeds, $v < v_F$, is strongly affected by the details of the adopted method, such as the treatment of the damping and the temperature effects. Let us now increase the distance from the charged particle to the top graphene layer. Figure 5 shows a comparison between the stopping and image forces, obtained by *ab initio* and MDF methods, for $b = 0.5$ nm and $b = 5$ nm. The Fermi energy of graphene sheets is $E_F = 200$ meV and the thickness of Al$_2$O$_3$ layer is $a = 5$ nm. Obviously, the electrostatic coupling between the opposite surfaces of our structure is no longer negligible for the distance $b = a = 5$ nm. One can see in Fig. 5 that the increase in b generally improves the agreement between the two methods for both the stopping and image forces over a wider range of speeds. This may be explained by referring to the discussion of Fig. 2(a) regarding the effects of high-energy interband electron transitions with energy ω_{high} in the *ab initio* method, from which we may conclude that improved agreement between the two methods may be expected in the range of speeds $v \lesssim 2b\omega_{\text{high}}$, which is expanded by increasing the distance b. However, there are differences in the stopping forces in Fig. 5(a) around $v = 1.5$–$2\ v_F$, where the *ab initio* method exhibits some local peak structures, which are not visible in the MDF method. Those structures can be assigned to a very sparse sampling of the *ab initio* energy loss function (ELF) in the region of small wave vectors for which it is still not possible to apply the ELF expression in the strict optical limit. As a result, the numerically obtained ELF could be notably discontinuous in the range of optically small wave vectors, thus possibly giving rise to artifacts, such as a shoulder and a small peak in the interval of speeds $v = 1.5$–$2\ v_F$ in the stopping force in Fig. 5(a), which are echoed by a small dip and a shoulder in the same interval of speeds in the image force in Fig. 5(b).

More interestingly, the local maximum in the stopping force at $v \approx 0.08\, v_F$ and the corresponding dip in the image force at about $v \approx 0.02$–$0.03\ v_F$, which were observed in the insets of Fig. 2 for $b = 0.5$ nm, are eliminated after the distance is increased to $b = 5$ nm, as shown in the insets of Figs. 5(a) and 5(b), respectively. This may be explained by the fact that, with the wave numbers that make the dominant contribution to the stopping force being reduced to the range $Q \lesssim 1/(2b) = 0.1\ \text{nm}^{-1}$, any fingerprint of the FK mode in the form of a sharp peak at a low speed $v \ll v_F$ is likely to be blurred by the Landau damping of that mode in the continuum of the intraband e-h excitations. This is to be expected based on the previously discussed conditions, because the cases with the distance $b = 5$ nm in Fig. 5 grossly violate the condition $b \lesssim (4k_F + \frac{2\omega_{\text{FK2}}}{v_F})^{-1} \approx 0.7$ nm. Instead of a sharp, phonon-induced peak, we observe in Fig. 5(a) a nonlinear behavior of the stopping force in the range of speeds $0 < v < v_F$, which could be loosely described as a very broad peak of the phononic origin being superimposed on a linear portion of the stopping force that comes from the intraband e-h excitations. The effects of increasing b on the FK phonon-induced peaks in the stopping force are further discussed in Sec. S2.A of the SM. Similar changes are also observed in the image force in Fig. 5(b), where the dip at the speedsof about 0.02–$0.03\ v_F$, seen in the inset to Fig. 2(b) for $b = 0.5$ nm, is eliminated after the distance is increased to $b = 5$ nm, so the image force becomes approximately constant at speeds $v \lesssim 0.1\ v_F$, as seen in the inset to Fig. 5(b). Next, we compare in Fig. 6 the stopping and image forces for two Al$_2$O$_3$ thicknesses, $a = 5$ nm and $a \to \infty$ (corresponding to a semi-infinite substrate), with the particle distance $b = 5$ nm, using the *ab initio* and MDF methods. This figure illustrates the effects of electrostatic coupling between the two surfaces, which were found in Fig. S2 of the SM to be negligible when $b = 0.5$ nm for the same two values of thickness a. In Fig. 6, we see that, when the distance is increased to $b = 5$ nm, the effects of the electrostatic coupling

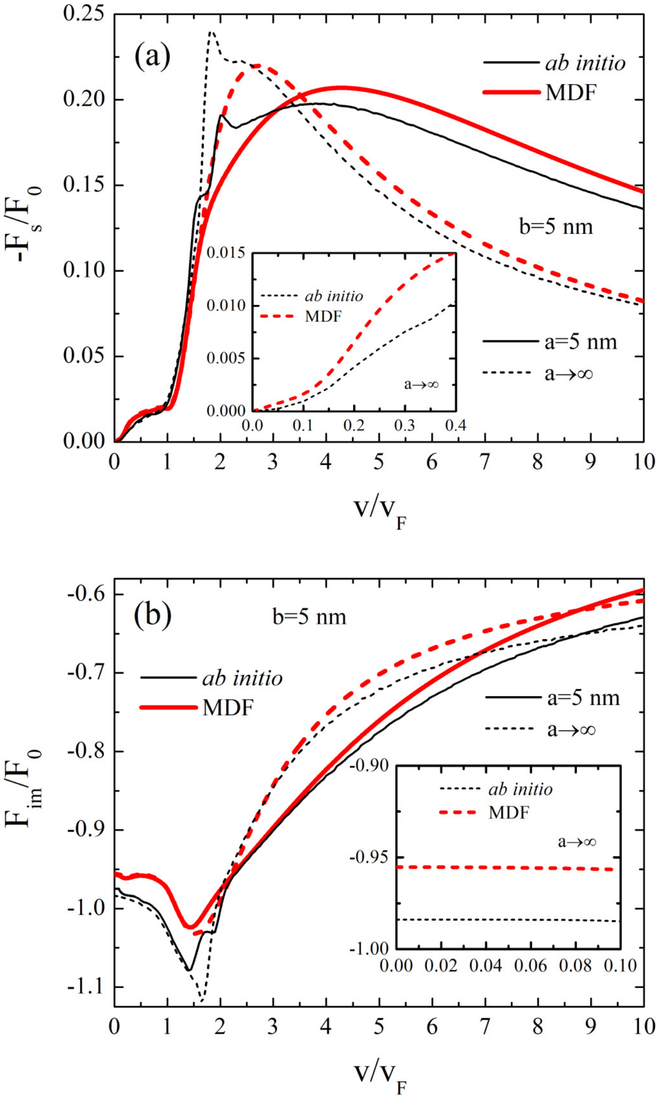

FIG. 6. The stopping force F_s (a) and the image force F_{im} (b), normalized by $F_0 = (Ze)^2/(4b^2)$, as functions of the speed v (normalized by v_F) of a charged particle moving at a distance $b = 5$ nm above the top graphene. The Fermi energy of graphene is $E_F = 200$ meV. Results are shown for two values of the $\mathrm{Al_2O_3}$ slab thicknesses: $a = 5$ nm (solid lines) and $a \to \infty$ (short dashed lines). Thin black lines are obtained using the *ab initio* method and thick red lines using the MDF method. The insets show the zoom of panels (a) and (b) in the low-velocity regime for a semi-infinite $\mathrm{Al_2O_3}$ substrate ($a \to \infty$).

are still strong at speeds $v \gtrsim 2\,v_F$. On the other hand, no effects of the increased thickness are observed in the stopping and image forces at the speeds $v \lesssim 1.5\,v_F$. Therefore, it appears that for the low-velocity behavior of those forces, where a strong interplay is expected between the phonon-induced hybrid modes and the continuum of the intraband e-h excitations takes place, the gr-$\mathrm{Al_2O_3}$-gr structure may be treated as a single graphene sheet on a semi-infinite substrate, even when $b \sim a$. This is somewhat surprising because the opposing surfaces of the gr-$\mathrm{Al_2O_3}$-gr structure should be electrostatically coupled for $a = b$. A possible explanation will be offered in Fig. 7, where the stopping force at speeds $v < v_F$ is dominated by the phononic modes of the antisymmetric type in a gr-$\mathrm{Al_2O_3}$-gr structure, which exhibit a series of avoided crossings in the range of the wavenumbers $Q \lesssim 0.1$ nm^{-1}, which look qualitative similar to the avoided crossings in a single graphene sheet on a semi-infinite substrate [29].

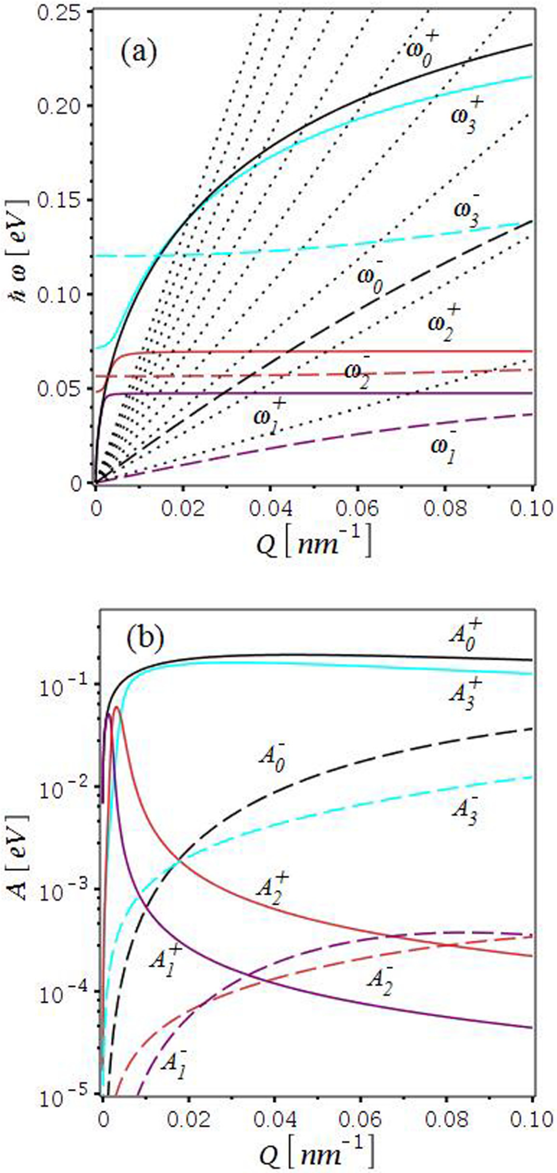

FIG. 7. The (a) resonant frequencies ω_j^p and (b) corresponding weights A_j^p are shown as functions of the wave number Q for two equally doped graphene sheets having the Fermi energy of $E_F = 200$ meV, a distance $a = 5$ nm apart, with (colored lines) and without (black lines) an $\mathrm{Al_2O_3}$ layer between them. The solid lines show the symmetric ($p = +$) and the dashed lines show antisymmetric ($p = -$) hybrid modes, with $j = 1$ (purple lines) and $j = 2$ (orange lines) labeling the lower-energy and higher-frequency phononic modes, and $j = 3$ (cyan lines) labeling the highest-frequency mode of plasmonic character. The ten black dotted lines in the panel (a) indicate the straight lines $\omega = vQ$, with the particle speed taking the values $v = v_F, 2v_F, \ldots, 10v_F$.

As noted in Fig. 5, the increase of the distance to $b = 5$ nm improves the agreement between the two methods for the stopping force in the case of $a \to \infty$ in Fig. 6 by expanding the range of speeds, $v \lesssim 2b\omega_{\text{high}}$, where high-energy interband transitions do not contribute to that force. On the other hand, there exists a difference between the two methods in the image force in the form of a constant shift at very low speeds, seen in the insets to both Figs. 5(b) and 6(b). This may be attributed to differences in the limit of static screening, which arise in the two methods because of the role of high-energy interband electron transitions in graphene's static polarizability, which are not included in the MDF method. Another possible source of the discrepancy may come from the effects of finite damping, which are not removed in the *ab initio* data according to Mermin's procedure.

B. Modal analysis and stopping force on two particles

To aid the discussion in this section, we present results of an analytical approximation for the modal decomposition of the ELF for a symmetrically doped gr-Al_2O_3-gr structure, developed in the SM. We also discuss in this subsection the stopping force for a somewhat more impractical, yet physically more revealing configuration of *two* charges moving in the *same direction* at equal speeds along parallel trajectories that are symmetrically located outside the structure.

In Figs. S1(a) and S1(b) in the SM, we have reproduced Figs. 6(a) and 7(b) from Ref. [36], showing the ELF, $\text{Im}[-1/\epsilon(\mathbf{Q},\omega)]$, for the gr-$\text{Al}_2\text{O}_3$-gr structure with $a = 5$ nm and $E_F = 200$ meV in two ranges of wave numbers, $Q < 0.08\ \text{nm}^{-1}$ and $Q < 0.8\ \text{nm}^{-1}$, respectively. Besides the density plots of the ELF obtained from the *ab initio* method, we also show in Fig. S1 the dispersion curves for various hybrid modes, calculated using the MDF method within the optical limit for graphene's response [36]. In the SM, we outline an analytical derivation of the modal decomposition of the ELF, achieved by neglecting all the damping mechanisms and using an approximation to the optical MDF model for the polarization function of doped graphene valid at long wavelengths, $Q \ll k_F$, and low frequencies, $\hbar\omega \lesssim E_F$, similar to the analysis performed in Ref. [91]. Using this approximation to solve the equation $\text{Re}[\epsilon(Q,\omega)] = 0$ gives analytical expressions for resonant frequencies, $\omega_j^p(Q)$, and the corresponding weight functions, $A_j^p(Q)$, appearing in Eq. (S15) of the SM, where $j = 1, 2, 3$ labels the hybrid modes with parity $p = \pm$ in a symmetrically doped gr-Al_2O_3-gr composite. With those expressions shown in Figs. 7(a) and 7(b), one may invoke Eqs. (S14) and (S15) of the SM to assess the contributions of various modes to the forces calculated in this section by noticing that the distance b of the charged particle reduces the range of the relevant wave numbers to $Q \lesssim 1/(2b)$, whereas the speed v of the charged particle controls the regions of the (Q,ω) plane, which contribute to the stopping force ($\omega < Qv$) and the image force ($\omega > Qv$), as discussed in Ref. [91]. To emphasize the role of this kinetic resonance condition in evaluation of the forces, we also show in Fig. 7(a) the straight lines $\omega = Qv$ for ten particle speeds, $v = v_F, 2v_F, \ldots, 10v_F$ (black dotted lines with increasing slope).

By choosing both equally and oppositely charged pairs of the comoving particles, which are symmetrically positioned with respect to the center of the sandwich at $z = 0$, we wish to achieve a selective excitation of the symmetric and antisymmetric hybridization of the plasmon/phonon modes in the gr-Al_2O_3-gr structure. When the Al_2O_3 layer is absent, the resulting double layer of equally doped graphene sheets supports a well-defined pair of plasmon modes in the domain $Qv_F < \omega < 2E_F - Qv_F$ for $0 < Q < k_F$, with a symmetric mode that retains the square-root dispersion relation akin to the DP in single-layer graphene, and an antisymmetric AP mode, which exhibits linear dispersion at long wavelengths, $\omega = Qv_{\text{ac,pl}}$ [see the black solid and dashed lines in Fig. 7(a), labeled ω_0^+ and ω_0^-, respectively] [33,34]. When the Al_2O_3 layer is present, it was shown in our previous publication [36] that a hybridization takes place between those two plasmonic modes in graphene sheets with two pairs of the surface optical phonon modes in the oxide slab, giving rise to altogether three symmetric [see the colored *solid* lines labeled by ω_j^+ for $j = 1, 2, 3$ in Fig. 7(a)] and three antisymmetric [see the colored *dashed* lines labeled by ω_j^- for $j = 1, 2, 3$ in Fig. 7(a)] modes. The dispersion curves of the three symmetric modes in Fig. 7(a) exhibit rapid variation due to a series of avoided crossings at long wavelengths, typically $Q < 0.01\ \text{nm}^{-1}$, whereas the three antisymmetric modes exhibit a generally much weaker dispersion at those wavelengths. As the wave number Q increases, the highest-energy symmetric mode and the highest-energy antisymmetric mode [labeled by ω_3^+ and ω_3^- in Fig. 7(a), respectively] regain the plasmonic character and continue to closely follow the dispersion relations of the symmetric and antisymmetric plasmon pair for two graphene sheets separated by a region with constant permittivity ϵ_{ox}^∞ [as can be seen in Fig S1(b) of the SM for the wave numbers $Q > 0.1\ \text{nm}^{-1}$]. At the same time, the dispersion relations of the two pairs of lower-energy symmetric [labeled by ω_1^+ and ω_2^+ in Fig. 7(a)] and antisymmetric [labeled by ω_1^- and ω_2^- in Fig. 7(a)] modes maintain their phononic character. As the wave number Q increases, those modes enter the continuum of the intraband e-h excitations [see the region $Q > \omega/v_F$ in Fig. 7(a)], where they become nearly degenerate ($\omega_j^- \to \omega_j^+$ for $j = 1, 2$) while undergoing attenuation due to Landau damping, and ultimately attain the energy of one of the two FK phonons in a Al_2O_3 surface ($\omega_j^+ \to \omega_{\text{FK}j}$ for $j = 1, 2$) as they emerge from that continuum [see the green horizontal lines in Fig. S1(b) of the SM at the wave numbers $Q > 2k_F + \omega/v_F \gtrsim 0.6\ \text{nm}^{-1}$], where they are statically screened by the graphene layers [36].

On the other hand, Fig. 7 exposes detailed behavior of all the hybrid modes in the long wavelength limit of particular interest for the stopping force, which should be enhanced in the presence of any acoustic modes in the gr-Al_2O_3-gr structure with equally doped graphene layers. In that context, it is shown in Sec. S2.B of the SM that for a thin structure, the lowest-energy antisymmetric mode [purple dashed line labeled by ω_1^- in Fig. 7(a)] exhibits linear dispersion in the limit $Q \to 0$ of the form $\omega = Qv_{\text{ac,ph}}$, with $v_{\text{ac,ph}} = e\sqrt{2aE_F/\epsilon_{ox}^0}$. When the Al_2O_3 layer is replaced with air, the resulting acoustic speed corresponds to the AP in double-layer graphene [black dashed line labeled by ω_0^- in Fig. 7(a)], which yields $v_{\text{ac,pl}} = e\sqrt{2aE_F} \approx 2.58\, v_F$ for the doping of $E_F = 200$ meV. In the presence of the Al_2O_3 layer, the acoustic mode is of a phononic character with a much reduced acoustic speed, $v_{\text{ac,ph}} \approx 0.73\, v_F$ for $E_F = 200$ meV, owing to the quite large value of the static permittivity of Al_2O_3, $\epsilon_{ox}^0 = 12.53$. We note that because $v_{\mathrm{ac,ph}} < v_F$, the dispersion relation of such an acoustic mode of the phononic origin is embedded in the continuum of the intraband e-h excitations in a range of the wave numbers $\omega/v_F < Q < 2k_F + \omega/v_F$, where that mode is exposed to Landau damping. With regard to the weights of various modes displayed in Fig. 7(b), it can be shown that the weight of the antisymmetric mode of the plasmonic type is much smaller than the weight of its symmetric counterpart for all particle speeds $v \gtrsim v_F$, both in a system with the Al_2O_3 layer, i.e., $A_3^- \ll A_3^+$, and a system without that layer, i.e., $A_0^- \ll A_0^+$. On the other hand, the weights of the symmetric phononic modes with $j = 1, 2$ are higher than the weights of their antisymmetric counterparts at high speeds, while this relation is reversed as the particle speed decreases. In Fig. 8, we discuss the case of two charges moving at equal speeds in the same direction along parallel trajectories that are located on the opposite sides of the gr-Al_2O_3-gr sandwich at equal distances b from the nearest graphene layers. We show results from the *ab initio* method for the stopping force on *one* of those particles when the accompanying particle is equally charged (F_s^+) and oppositely charged (F_s^-) for two distances: (a) $b = 5$ nm and (b) $b = 50$ nm. For the sake of comparison, we also show the usual stopping force on a single charged particle (F_s) moving at the same velocity and distance as those two particles. As expected from Eq. (23), the stopping force F_s on a single charged particle is an arithmetic mean of the stopping forces F_s^+ and F_s^-, whereas their half difference, $F_c \approx (F_s^+ - F_s^-)/2$, is a measure of the electrostatic coupling between the opposite surfaces of our sandwich structure. We consider in Fig. 8 that graphene layers are equally doped with $E_F = 200$ meV and are placed a distance $a = 5$ nm apart, with and without an Al_2O_3 layer between them. The SM shows that the electrostatic coupling between the graphene layers should be strong with this choice of the a and b values.

In Fig. 8(a), we see that an inequality $|F_s^+| > |F_s^-|$ holds for the gr-Al_2O_3-gr system at high speeds, $v \gtrsim 2\,v_F$. Moreover, the shape of the velocity dependence of the force F_s^+ at speeds $v \gtrsim 2v_F$ supports the previously discussed notion that stopping is likely dominated by the highest-lying symmetric, the DP-like hybrid mode, whose square-root dispersion ω_3^+ gives rise to a broad maximum at speeds 4–5 v_F, similar to that in Fig. 6(a). It is then conceivable that the force F_s^- stems from the highest-lying antisymmetric mode ω_3^- in the range of speeds $v \gtrsim 2v_F$, so the inequality $|F_s^+| > |F_s^-|$ seems to reflect the fact that the symmetric hybrid mode of plasmonic type occurs at a generally higher frequency, and that it contributes to the ELF with a larger weight than the corresponding antisymmetric mode of plasmic type [see the solid and dashed cyan curves in Fig. 7(b)]. A similar conclusion may be drawn from the shapes of the stopping curves F_s^+ and F_s^- for the case without the Al_2O_3 layer at speeds $v \gtrsim 2.5\,v_F$.

On the other hand, the fact that the maxima in the stopping forces F_s^-, which are observed at speeds 1.5–2 v_F in Fig. 8(a) both with and without the Al_2O_3 layer, are much narrower than the maxima in the corresponding forces F_s^+, is commensurate with the perceived enhancement of the energy loss when the resonance condition is met, i.e., when the particle speed matches the acoustic speed of a linearly dispersing mode. This is readily corroborated for F_s^- in the case without the Al_2O_3 layer, where we observe a peak at $v \approx 2\,v_F$, which is somewhat smaller than the acoustic speed of the AP in double-layer graphene, $v_{\mathrm{ac,pl}} \approx 2.58\,v_F$ [33], the difference being probably because the AP dispersion tends to saturate as Q surpasses the value ∼0.1 nm^{-1} (see Fig. 5 in Ref. [36]). However, the origin of a narrow peak in F_s^- at about $v = 1.5\,v_F$ in the presence of the Al_2O_3 layer is not immediately obvious, but it may be traced to the highest-lying antisymmetric hybrid mode because its dispersion relation ω_3^- approaches that of an AP with the screened acoustic

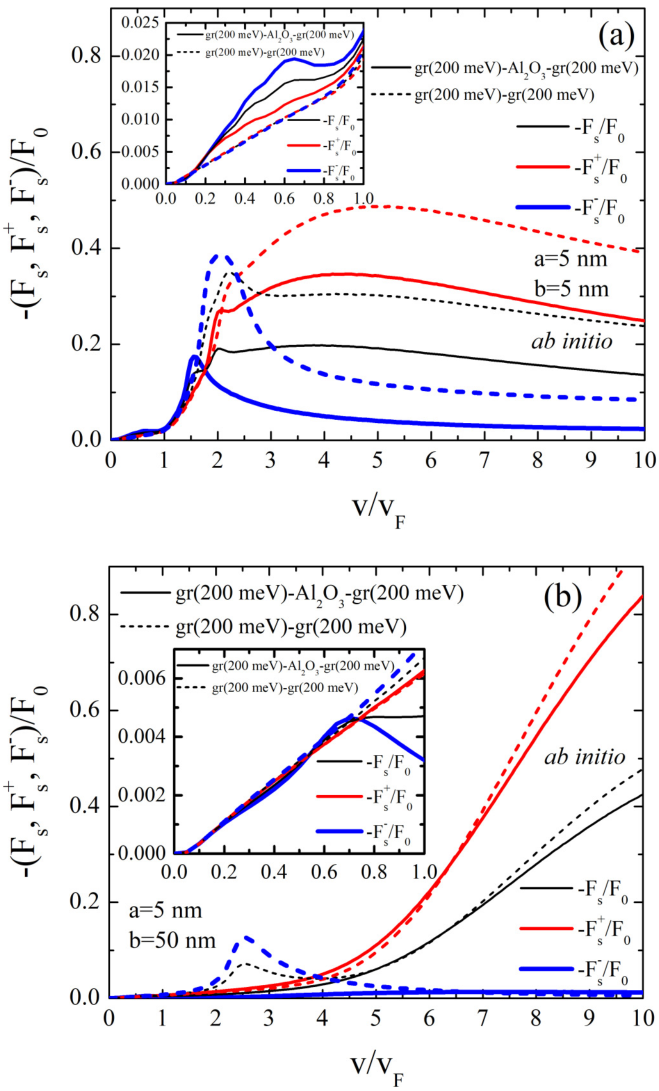

FIG. 8. The stopping forces F_s (thin black lines), F_s^+ (medium red lines), and F_s^- (thick blue lines), normalized by $F_0 = (Ze)^2/(4b^2)$ as functions of speed v (normalized by v_F) of a charged particle moving at two distances above the top graphene: (a) $b = 5$ nm and (b) $b = 50$ nm, obtained using the *ab initio* method. The separation between graphene layers (or the Al_2O_3 slab thickness) is $a = 5$ nm and both layers are doped such that $E_F = 200$ meV. Results are shown for two composite systems: gr-Al_2O_3-gr (solid lines) and gr-gr (short dashed lines). The insets show the zoom of panels (a) and (b) in the low-velocity regime.

speed $v_{\rm ac,pl} = e\sqrt{2aE_F/\epsilon_{ox}^{\infty}} \approx 1.44\,v_F$ arising for two sheets of graphene doped with $E_F = 200$ meV and separated by a region of thickness $a = 5$ nm with the dielectric constant of $\epsilon_{ox}^{\infty} = 3.2$ [see Fig. S1(b) in the SM at $Q \gtrsim 0.1$ nm^{-1}].

Furthermore, a reversed inequality, $|F_s^-| > |F_s^+|$, holds at low speeds, $v < v_F$, in the case with the $\mathrm{Al_2O_3}$ layer, as shown in the inset to Fig. 8(a). Given that this range of speeds is dominated by the phononic hybrid modes, which are quenched by Landau damping in the continuum of the intraband e-h excitations, the reversal of the roles of the symmetric and antisymmetric modes may be explained by noticing that $A_1^- > A_1^+$ in Fig. 7(b) for $Q \gtrsim 0.035$ nm^{-1}, so the linearly dispersing portion of ω_1^- for the lowest-energy antisymmetric mode is still dominant over its weakly dispersing symmetric counterpart with ω_1^+, even after they are both heavily broadened by the Landau damping. In that respect, the broad maximum in F_s^- at about $v = 0.6\,v_F$ in the inset to Fig. 8(a) may be considered a weak signature of the acoustic behavior of the phononic mode, with ω_1^- exhibiting the acoustic speed $v_{\rm ac,ph} \approx 0.73\,v_F$ at long wavelengths. At the same time, as discussed in Fig. 5, the distance $b = 5$ nm in Fig. 8(a) is too large to allow for the appearance of a sharp peak in either of the stopping forces $F_s^{\pm}$, which would originate from the nondispersing portions of the higher-energy phononic modes with the dispersions $\omega_2^{\pm}$ that extend to the wave numbers beyond the continuum of the intraband e-h excitations. We see in the inset of Fig. 8(a) that, in the case without the $\mathrm{Al_2O_3}$ layer, $F_s^- \approx F_s^+ \approx F_s$ at low speeds, $v < v_F$, because of the absence of phonon modes, whereas the linear increase of all three stopping forces indicates the familiar regime of friction due to the excitation of the intraband e-h pairs in graphene.

Finally, by choosing a rather large distance $b = 50$ nm in Fig. 8(b), we suppress contributions to the stopping force coming from the wave numbers exceeding $Q \sim 1/(2b) = 0.01$ nm^{-1}. One may observe in Fig. 7 that, in the range $Q \lesssim 0.01$ nm^{-1}, the weights of all antisymmetric modes are significantly reduced in comparison with the weights of their symmetric counterparts, whereas all the symmetric modes have comparable weights and exhibit avoided crossings in that range, which can only be probed by a stopping force at speeds exceeding $v = 10\,v_F$, i.e., beyond the range of speeds discussed in this paper. Nevertheless, we can still provide a semiquantitative discussion of the results shown in Fig. 8(b) in the range of speeds $v < 10\,v_F$ by noticing that, owing to the inequality $Qa \sim a/(2b) \ll 1$, the whole sandwich structure may be considered optically thin [93]. Accordingly, we have developed in Sec. S2.B of the SM an approximate modal decomposition of the ELF for a thin structure, which gives rise to two dominant modes at wave numbers $Q \lesssim 0.01$ nm^{-1}: a higher-energy, symmetric mode with frequency $\omega_{\rm DP}(Q) = e\sqrt{2QE_F^*}$, which describes the DP in a single, free-standing graphene sheet with doubled Fermi energy, $E_F^* = 2E_F$, and a lower-energy, antisymmetric, linearly dispersing mode with the acoustic speed of $v_{ac} = e\sqrt{2aE_F/\epsilon_S(0)}$. It is shown in the SM that, in the range of wave numbers $Q \lesssim 0.01$ nm^{-1}, the curve $\omega = \omega_{\rm DP}(Q)$ approximates the dispersion relation of the mode ω_0^+ in Fig. 7(a) for a structure without the $\mathrm{Al_2O_3}$ layer and it interpolates across the dispersion curves of all three symmetric modes in a structure with that layer. At the same time, the line $\omega = v_{ac}Q$ is found to reproduce the linearly dispersing portions of the antisymmetric modes ω_0^- or ω_1^- in Fig. 7(a) for $Q \lesssim 0.01$ nm^{-1} when its acoustic speed $v_{\rm ac}$ is evaluated by setting $\epsilon_S(0) = 1$ or $\epsilon_S(0) = \epsilon_{ox}^0 = 12.53$, respectively.

In Fig. 8(b), we see that the forces F_s^+ are almost the same for the cases with and without the $\mathrm{Al_2O_3}$ layer, pointing to the fact that they are dominated by the DP-like mode with frequency $\omega_{\rm DP}(Q)$, which is independent of the thickness a and of the dielectric constant of the material between the two graphene sheets, as expected in an optically thin material [93]. Moreover, the fact that the curves F_s^+ keep increasing with increasing speed may be explained by referring to the analytical result for the stopping force, given in Eq. (S23) of the SM, which implies that a maximum of that force should occur at the speed $v_p \approx 1.7\,e\sqrt{bE_F^*}$, taking a value $v_p \approx 13.9\,v_F$ that lies just outside the range of speeds shown in Fig. 8(b) (see the red dashed curve in Fig. S4 of the SM). At the same time, the force F_s^- in the case with the $\mathrm{Al_2O_3}$ layer is almost diminished in Fig. 8(b) at speeds $v_F \lesssim v \lesssim 10\,v_F$. This is consistent with the fact, seen in Fig. 7, that the weights of all antisymmetric modes are suppressed when probed in the very long wavelength regime by the stopping force at such a large distance as $b = 50$ nm. On another note, the force F_s^- in Fig. 8(b) in the case without the $\mathrm{Al_2O_3}$ layer shows a narrow, strongly asymmetric peak close to the acoustic speed of on AP $v_{\rm ac} = v_{\rm ac,pl} \approx 2.58\,v_F$. It is argued in Sec. S2.B of the SM that the asymmetric shape of that peak is a reflection of the square-root singularity $\sim 1/\sqrt{v - v_{ac,pl}}$ in the force in Eq. (S24) (see the blue dashed curve in Fig. S4 of the SM), and may thus be considered a signature of the AP in an optically thin structure consisting of two graphene sheets without the $\mathrm{Al_2O_3}$ layer. Similarly, the peak seen in the force F_s^- in Fig. 8(b) at about $v_{\rm ac} = v_{\rm ac,ph} \approx 0.73\,v_F$ in the presence of the $\mathrm{Al_2O_3}$ layer is likely related to the phononic acoustic mode ω_1^-, but is distorted by the presence of the continuum of the intraband e-h excitations.

A comparison between all force components at the speeds $0 < v < v_F$ in the inset to Fig. 8(b) reveals some interesting features. They all have the same magnitude and exhibit a linear increase at speeds $0 < v \lesssim v_{\rm ac,ph} \approx 0.73\,v_F$, both with and without the $\mathrm{Al_2O_3}$ layer, attesting to a dominant role of the continuum of the intraband e-h excitations, which cannot be described by a simple modal decomposition that ignores all damping mechanisms. All the force components continue to increase in the same manner for $v \gtrsim 0.73\,v_F$, except for F_s^- in the case with the $\mathrm{Al_2O_3}$ layer, which switches to a linearly decreasing form in such a manner that the total stopping force F_s appears approximately constant for $v \gtrsim 0.73\,v_F$. This results in a peculiar triangular shape of the peak region of F_s^- at speeds around $v_{\rm ac,ph} \approx 0.73\,v_F$ in the case with the $\mathrm{Al_2O_3}$ layer. We speculate that this scenario results from an interplay between the linearly dispersing portion of the phononic mode ω_1^- with the continuum of the intraband e-h excitations at very long wavelengths, which requires a broader analysis. A further discussion of this point is provided in the concluding paragraph of the SM.

IV. CONCLUDING REMARKS

We have performed a thorough analysis of the stopping and image forces on a charged particle moving parallel to a gr-$\mathrm{Al_2O_3}$-gr sandwich structure, covering broad ranges of the particle speeds and distances, as well as the doping densities of the two graphene sheets. This analysis relies on our previous work [36], where a detailed discussion of the ELF was presented in the (Q, ω) plane for the same structure, based on extensive calculations using the *ab initio* and MDF methods for the dynamic response of the structure. While the *ab initio* method includes features in the ELF coming from the high-energy interband electron transitions in graphene, we focus in this paper on the THz-MIR range of frequencies, where the MDF method should provide a useful analytical approximation. Using those two methods to compute the stopping and image forces constitutes a step toward proposing a spectroscopy based on an electron or ion beam under aloof, or grazing incidence upon the gr-$\mathrm{Al_2O_3}$-gr structure, which may provide additional insight into the plasmon-phonon hybridization processes in that structure. Such a spectroscopy offers an attractive possibility to tune both the particle's speed v and its distance b to probe the dispersion relations of various hybrid modes in the (Q, ω) plane. In particular, controlling the distance b enables the control of the range of wave numbers, $Q \lesssim 1/(2b)$, that contribute to the stopping and image forces. On the other hand, by varying the speed, one may control the complementary segments of the (Q, ω) plane, which contribute to the stopping force ($\omega < Qv$) and to the image force ($\omega > Qv$) [91].

In our paper, we addressed several interesting questions.

(1) We paid special attention to the acoustic type of hybrid modes, which exhibit linear dispersion at long wavelengths, because the stopping force should be particularly enhanced at a particle speed that matches the acoustic speed of such modes. In particular, we have identified two types of acoustic modes, exhibiting plasmonic and phononic characters, and searched for their signatures in the stopping force.

(2) We discussed at length the regime of low particle speeds, below the Fermi speed of graphene v_F, where a signature of the optical phonon modes in the $\mathrm{Al_2O_3}$ layer is expected to arise, and we analyzed their interaction with the continuum of the intraband e-h excitation in doped graphene, which is normally responsible for the friction regime of a stopping force.

(3) Besides calculations of the stopping force on a single incident charged particle, we also studied in some detail the case of two comoving particles with equal or opposite charges, which can be used to selectively excite the symmetric or antisymmetric hybrid modes in a gr-$\mathrm{Al_2O_3}$-gr structure with equally doped graphene sheets. While this configuration of the incident particles is more challenging to realize in practice, it provides an indirect insight into the relative weights of those two types of modes in the ELF of the structure.

(4) By a direct comparison of the results obtained with the *ab initio* and MDF methods, we have assessed the domain of the applicability of the MDF method for the stopping and image force calculations, and we discussed the significance of the model parameters, such as the damping and temperature.

Among other findings, we made the following observations regarding the stopping and image forces in terms of parameters v, b, a, and E_F.

(1) Both the stopping and image forces exhibit the dependencies on the speed in the region $v > v_F$, which are dominated by the highest-energy, plasmonic hybrid mode with a square-root dispersion, akin to the DP in graphene.

(2) At speeds $v < v_F$, the stopping force without the $\mathrm{Al_2O_3}$ layer exhibits a linear increase with v, corresponding to the regime of friction due to the continuum of the low-energy intraband e-h excitations in graphene.

(3) In the presence of an $\mathrm{Al_2O_3}$ layer, there is generally a shift of weight in the stopping force, with its magnitude reduction in the high-speed region, $v > v_F$, and an increase of the phonon-induced features in the low-speed region, $v < v_F$.

(4) A signature of a nondispersing FK phonon mode in the $\mathrm{Al_2O_3}$ layer can be observed as a sharp peak in the stopping force (or a narrow dip in the image force) at a very low speed $v \ll v_F$ for sufficiently small distance b, satisfying the conditions in Eq. (25). That signature results from the portion of the FK dispersion lying outside the continuum of the intraband e-h excitations in graphene.

(5) As the doping density of graphene increases, there is a redistribution of the weights in the stopping force in the region $v < v_F$, with the FK phonon-induced peak being suppressed and a linearly increasing force taking over at the speeds approaching v_F from below.

(6) When $a \gg b$, the electrostatic coupling between the modes in the opposing surfaces of the gr-$\mathrm{Al_2O_3}$-gr structure is weak and the forces exhibit the features analyzed for the system of a single graphene sheet on a semi-infinite $\mathrm{Al_2O_3}$ substrate.

(7) When b increases so $a \sim b$, the sharp peak in the stopping force at $v \ll v_F$ disappears in the case with the $\mathrm{Al_2O_3}$ layer, and the region $0 < v < v_F$ exhibits a nonlinear dependence of the speed, indicating an interplay of the intraband e-h excitations in graphene and an acoustic mode of the phononic type with its dispersion relation embedded in the continuum of these excitations.

(8) The results for the stopping force from the MDF method are found in generally good agreement with those from the *ab initio* method for the speeds and distances satisfying the relation $v \lesssim 2b\omega_{\mathrm{high}}$, where ω_{high} is a typical energy of the high-energy interband electron transitions, which are included in the *ab initio* method but not in the MDF method.

(9) There are systematic differences between the two methods in the image force values at low speeds, $v \ll v_F$, which may be attributed to differences in the limit of static screening, where the static polarizability of graphene includes the high-energy interband electron transitions in the *ab initio* method but not in the MDF method.

(10) The MDF method provides a generally good description of the interaction of the phononic modes and the intraband e-h excitations in the stopping force at speeds $v < v_F$, but the modeling in that range is sensitive to the temperature effects and the treatment of the phenomenological damping.

(11) A necessary condition for the appearance of an acoustic mode with linear dispersion at long wavelengths is $a \ll b$, which promotes the use of the optical limit for graphene's

response function and allows one to treat the gr-Al_2O_3-gr sandwich structure as optically thin.

(12) In the case of a comoving pair of incident particles with equal/opposite charges at $b = a$, the shapes of the maxima in the stopping forces per particle that occur at speeds $v > v_F$ show evidence of the highest-energy symmetric mode of plasmonic type with a DP-like square-root dispersion and the highest-energy antisymmetric mode of plasmonic type, AP, which exhibits acoustic dispersion at long wavelengths.

(13) For the comoving pair of charged particles in the case $b = a$, the stopping force exhibits a nonlinear dependence on speed in the region $v < v_F$, with a dominant contribution coming from the lowest-energy antisymmetric mode of phononic type, exhibiting acoustic dispersion that is embedded in the continuum of the intraband e-h excitations.

(14) For the comoving pair of charged particles in the case $b \gg a$ without the Al_2O_3 layer, the stopping force shows evidence of the DP–AP pair of hybrid modes, whereas in the presence of the Al_2O_3 layer, the stopping force from all the antisymmetric modes is quenched for $v \gtrsim v_F$.

We attempted to support our discussion of the results obtained from the *ab initio* and MDF methods by the results from simplified analytical models for a modal decomposition of the ELF, which were developed in the SM in certain limiting parameter regions of a general gr-Al_2O_3-gr structure. In particular, we have found analytical expressions for the stopping forces' origination from (a) the FK phononic modes in a thick structure with lightly doped graphene, given in Eq. (S21), as well as (b) the Dirac-like plasmon, and (c) AP in a thin structure, given in Eqs. (S23) and (S24), respectively. In the case of an AP of the phononic type in a thin gr-Al_2O_3-gr structure, further work is needed to achieve an analytical description of the interaction of such plasmons with the continuum of the intraband e-h excitations. Perhaps the methods of contour integral representation in the scattering problems of electromagnetic theory could be generalized to tackle such a task [94,95].

While the role of ELF is well-established in various EELS techniques, we wish to point to the importance of including the stopping and image forces in the particle scattering trajectory simulations, especially at low incident speeds, large distances, and grazing-angle incidence. The connection of both the stopping and image forces with modal decomposition of the ELF, which is demonstrated in the SM for this paper and in a previous work [91], opens the possibility to relate the total energy loss and the beam deflection angles to the particle scattering trajectories for certain EELS techniques. Such a relation could be possibly used to design experiments with the goal of detecting a specific mode. For example, our simple analysis of the peaks in the velocity dependence of the stopping force originated in the acoustic and DP modes in a graphene double layer, outlined in Sec. S2.B of the SM, is based on certain constraints on the system parameters and the particle scattering regime. Obviously, more future work is required to conduct realistic particle trajectory simulations using the forces discussed in this paper. Such a project would be most appropriately of interest for REELS under glancing angles [73–75] as well as for LEIGS [76–79]. For the former technique, the dependence of the derived ELF on scattering conditions has been identified as an open issue [96] whereas, for the latter technique, using low-energy protons raises questions regarding the charge-state evolution during scattering [97].

ACKNOWLEDGMENTS

This research is funded by the Ministry of Education, Science and Technological Development of the Republic of Serbia and the Serbia-Croatia bilateral project (Grant No. 337-00-205/2019-09/28). A.K., V.D., I.R., and L.K. would like to acknowledge networking support from COST Action CA19118EsSENce, supported by the COST Association (European Cooperation in Science and Technology). V.D. acknowledges financial support from Croatian Science Foundation (Grant No. IP-2020-02-5556) and European Regional Development Fund for the QuantiXLie Centre of Excellence (Grant No. KK.01.1.1.01.0004). Computational resources were provided by the Donostia International Physics Center (DIPC) computing center. Z.L.M. acknowledges financial support from the Natural Sciences and Engineering Research Council of Canada (Grant No. 2016-03689).

[1] K. S. Novoselov, A. K. Geim, V. S. Morozov, D. Jiang, Y. Zhang, V. S. Dubonos, V. I. Grigorieva, and A. A. Firsov, Science **306**, 666 (2004).

[2] S. K. Tiwari, S. Sahoo, N. Wang, and A. Huczko, J. Sci. Adv. Mater. Devices **5**, 10 (2020).

[3] K. S. Novoselov, A. K. Geim, V. S. Morozov, D. Jiang, M. I. Katsnelson, V. I. Grigorieva, V. S. Dubonos, and A. A. Firsov, Nature (London) **438**, 197 (2005).

[4] Y. Zhang, Y. W. Tan, H. L. Stormer, and P. Kim, Nature (London) **438**, 201 (2005).

[5] V. Kaydashev, B. Khlebtsov, A. Miakonkikh, E. Zhukova, S. Zhukov, D. Mylnikov, I. Domaratskiy, and D. Svintsov, Nanotechnology **32**, 035201 (2021).

[6] K. Lyon, D. J. Mowbray, and Z. L. Mišković, Ultramicroscopy **214**, 113012 (2020).

[7] T. Djordjević, I. Radović, V. Despoja, K. Lyon, D. Borka, and Z. L. Mišković, Ultramicroscopy **184**, 134 (2018).

[8] V. Despoja, J. Jakovac, N. Golenić, and L. Marušić, npj 2D Mater. Appl. **4**, 19 (2020).

[9] V. Despoja, I. Radović, A. Politano, and Z. L. Mišković, Nanomaterials **10**, 703 (2020).

[10] N. Zhang, X. Jiang, J. Fan, W. Luo, Y. Xiang, W. Wu, M. Ren, X. Zhang, W. Cai, and J. Xu, Nanotechnology **30**, 505201 (2019).

[11] Y. Fan, N. H. Shen, F. Zhang, Q. Zhao, H. Wu, Q. Fu, Z. Wei, H. Li, and C. M. Soukoulis, Adv. Opt. Mater. **7**, 1800537 (2019).

[12] V. Despoja, D. Novko, I. Lončarić, N. Golenić, L. Marušić, and V. M. Silkin, Phys. Rev. B **100**, 195401 (2019).

[13] A. Politano, H. K. Yu, D. Farías, and G. Chiarello, Phys. Rev. B **97**, 035414 (2018).

[14] A. Politano, I. Radović, D. Borka, Z. L. Mišković, H. K. Yu, D. Farías, and G. Chiarello, Carbon **114**, 70 (2017).

[15] A. Politano, I. Radović, D. Borka, Z. L. Mišković, and G. Chiarello, Carbon **96**, 91 (2016).

[16] S. Das Sarma, S. Adam, E. H. Hwang, and E. Rossi, Rev. Mod. Phys. **83**, 407 (2011).

[17] A. H. Castro Neto, F. Guinea, N. M. R. Peres, K. S. Novoselov, and A. K. Geim, Rev. Mod. Phys. **81**, 109 (2009).

[18] D. Novko, V. Despoja, and M. Šunjić, Phys. Rev. B **91**, 195407 (2015).

[19] M. Jablan, H. Buljan, and M. Soljačić, Phys. Rev. B **80**, 245435 (2009).

[20] F. Bonaccorso, Z. Sun, T. Hasan, and A. C. Ferrari, Nat. Photonics **4**, 611 (2010).

[21] A. Vakil and N. Engheta, Science **332**, 1291 (2011).

[22] T. Low and P. Avouris, ACS Nano **8**, 1086 (2014).

[23] H. Yan, X. Li, B. Chandra, G. Tulevski, Y. Wu, M. Freitag, W. Zhu, P. Avouris, and F. Xia, Nat. Nanotechnol. **7**, 330 (2012).

[24] J. S. Gomez-Diaz, C. Moldovan, S. Capdevila, J. Romeu, L. S. Bernard, A. Magrez, A. M. Ionescu, and J. Perruisseau-Carrier, Nat. Commun. **6**, 6334 (2015).

[25] Y. Francescato, V. Giannini, J. Yang, M. Huang, and S. A. Maier, ACS Photonics **1**, 437 (2014).

[26] V. M. Fischetti, D. A. Neumayer, and E. A. Cartier, J. Appl. Phys. **90**, 4587 (2001).

[27] H. Yan, T. Low, W. Zhu, Y. Wu, M. Freitag, X. Li, F. Guinea, P. Avouris, and F. Xia, Nat. Photonics **7**, 394 (2013).

[28] Z. Fei, G. O. Andreev, W. Bao, L. M. Zhang, A. S. McLeod, C. Wang, M. K. Stewart, Z. Zhao, G. Dominguez, M. Thiemens *et al.*, Nano Lett. **11**, 4701 (2011).

[29] T. Marinković, I. Radović, D. Borka, and Z. L. Mišković, Plasmonics **10**, 1741 (2015).

[30] P. Alonso-González, A. Y. Nikitin, Y. Gao, A. Woessner, M. B. Lundeberg, A. Principi, N. Forcellini, W. Yan, S. Vélez, A. J. Huber *et al.*, Nat. Nanotechnol. **12**, 31 (2017).

[31] I.-H. Lee, D. Yoo, P. Avouris, T. Low, and S.-H. Oh, Nat. Nanotechnol. **14**, 313 (2019).

[32] L. Marušić, A. Kalinić, I. Radović, J. Jakovac, Z. L. Mišković, and V. Despoja, IJMS **23**, 4770 (2022).

[33] E. H. Hwang and S. Das Sarma, Phys. Rev. B **80**, 205405 (2009).

[34] R. E. V. Profumo, R. Asgari, M. Polini, and A. H. MacDonald, Phys. Rev. B **85**, 085443 (2012).

[35] C. Wen, J. Luo, W. Xu, Z. Zhu, S. Qin, and J. Zhang, Biosensors **11**, 431 (2021).

[36] V. Despoja, T. Djordjević, L. Karbunar, I. Radović, and Z. L. Mišković, Phys. Rev. B **96**, 075433 (2017).

[37] F. J. García de Abajo and P. M. Echenique, Phys. Rev. B **46**, 2663 (1992).

[38] D. J. Mowbray, Z. L. Mišković, F. O. Goodman, and Y. N. Wang, Phys. Lett. A **329**, 94 (2004).

[39] Y. N. Wang and T. C. Ma, Phys. Rev. B **52**, 16395 (1995).

[40] I. Radović, D. Borka, and Z. L. Mišković, Phys. Lett. A **375**, 3720 (2011).

[41] V. Despoja, K. Dekanić, M. Šunjić, and L. Marušić, Phys. Rev. B **86**, 165419 (2012).

[42] I. Radović, D. Borka, and Z. L. Mišković, Phys. Rev. B **86**, 125442 (2012).

[43] I. Radović, D. Borka, and Z. L. Mišković, Phys. Lett. A **377**, 2614 (2013).

[44] X. Shi, X. Lin, F. Gao, H. Xu, Z. Yang, and B. Zhang, Phys. Rev. B **92**, 081404(R) (2015).

[45] A. J. Chaves, N. M. R. Peres, G. Smirnov, and N. A. Mortensen, Phys. Rev. B **96**, 195438 (2017).

[46] E. B. Kolomeisky and J. P. Straley, Phys. Rev. Lett. **120**, 226801 (2018).

[47] X. J. Bai, Y. Y. Zhang, Z. L. Mišković, I. Radović, C. Z. Li, and Y. H. Song, Plasmonics **16**, 1089 (2021).

[48] X. L. He, Y. Y. Zhang, Z. L. Mišković, I. Radović, C. Z. Li, and Y. H. Song, Eur. Phys. J. D **74**, 18 (2020).

[49] C. Z. Li, S. R. Na, Y. Y. Jian, Y. N. Wang, and Z. L. Mišković, Radiat. Eff. Defects Solids **174**, 19 (2019).

[50] I. Radović, L. Hadžievski, N. Bibić, and Z. L. Mišković, Mater. Chem. Phys. **118**, 293 (2009).

[51] I. Radović and D. Borka, Phys. Lett. A **374**, 1527 (2010).

[52] K. F. Allison and Z. L. Mišković, Nanotechnology **21**, 134017 (2010).

[53] D. Borka, I. Radović, and Z. L. Mišković, Nucl. Instrum. Methods Phys. Res., Sect. B **269**, 1225 (2011).

[54] I. Radović, V. Borka Jovanović, D. Borka, and Z. L. Mišković, Nucl. Instrum. Methods Phys. Res., Sect. B **279**, 165 (2012).

[55] C. Z. Li, Y. N. Wang, Y. H. Song, and Z. L. Mišković, Phys. Lett. A **378**, 1626 (2014).

[56] S. Segui, J. L. Gervasoni, N. R. Arista, and Z. L. Mišković, Nucl. Instrum. Methods Phys. Res., Sect. B **490**, 18 (2021).

[57] I. Radović, L. Hadžievski, N. Bibić, and Z. L. Mišković, Phys. Rev. A **76**, 042901 (2007).

[58] J. Zuloaga, Z. L. Mišković, and F. O. Goodman, Nucl. Instrum. Methods Phys. Res., Sect. B **256**, 162 (2007).

[59] I. Radović, L. Hadžievski, and Z. L. Mišković, Phys. Rev. B **77**, 075428 (2008).

[60] K. F. Allison, D. Borka, I. Radović, L. Hadžievski, and Z. L. Mišković, Phys. Rev. B **80**, 195405 (2009).

[61] J. Niu, Y. Jun Shin, Y. Lee, J. H. Ahn, and H. Yang, Appl. Phys. Lett. **100**, 061116 (2012).

[62] M. Liu, X. Yin, and X. Zhang, Nano Lett. **12**, 1482 (2012).

[63] B. Xiao, R. Sun, Z. Xie, and X. Wang, Optoelectron. Adv. Mater., Rapid Commun. **9**, 692 (2015).

[64] V. Despoja, I. Radović, L. Karbunar, A. Kalinić, and Z. L. Mišković, Phys. Rev. B **100**, 035443 (2019).

[65] A. Kalinić, I. Radović, L. Karbunar, V. Despoja, and Z. L. Mišković, Phys. E **126**, 114447 (2021).

[66] A. Kalinić, I. Radović, L. Karbunar, V. Despoja, and Z. L. Mišković, Publ. Astron. Obs. Belgrade **99**, 97 (2020).

[67] O. Stephan, D. Taverna, M. Kociak, K. Suenaga, L. Henrard, and C. Colliex, Phys. Rev. B **66**, 155422 (2002).

[68] C. Kramberger, R. Hambach, C. Giorgetti, M. H. Rümmeli, M. Knupfer, J. Fink, B. Büchner, L. Reining, E. Einarsson, S. Maruyama *et al.*, Phys. Rev. Lett. **100**, 196803 (2008).

[69] T. Eberlein, U. Bangert, R. R. Nair, R. Jones, M. Gass, A. L. Bleloch, K. S. Novoselov, A. Geim, and P. R. Briddon, Phys. Rev. B **77**, 233406 (2008).

[70] Y. Susuki, H. Mukai, K. Kimura, and M. Mannami, Nucl. Instrum. Methods Phys. Res., Sect. B **48**, 347 (1990).

[71] H. Winter, J. C. Poizat, and J. Remillieux, Nucl. Instrum. Methods Phys. Res., Sect. B **67**, 345 (1992).

[72] P. A. Crozier, Ultramicroscopy **180**, 104 (2017).

[73] Y. Liu, R. F. Willis, K. V. Emtsev, and T. Seyller, Phys. Rev. B **78**, 201403(R) (2008).

[74] Y. Liu and R. F. Willis, Phys. Rev. B **81**, 081406(R) (2010).

[75] A. Politano and G. Chiarello, Nanoscale **6**, 10927 (2014).

[76] A. G. Borisov, A. Mertens, H. Winter, and A. K. Kazansky, Phys. Rev. Lett. **83**, 5378 (1999).

[77] J. Villette, A. G. Borisov, H. Khemliche, A. Momeni, and P. Roncin, Phys. Rev. Lett. **85**, 3137 (2000).

[78] A. A. Lucas, M. Šunjić, and G. Benedek, J. Phys.: Condens. Matter **25**, 355009 (2013).

[79] A. A. Lucas, M. Šunjić, G. Benedek, and P. M. Echenique, New J. Phys. **16**, 063015 (2014).

[80] V. Despoja, D. Novko, K. Dekanić, M. Šunjić, and L. Marušić, Phys. Rev. B **87**, 075447 (2013).

[81] See Supplemental Material at http://link.aps.org/supplemental/10.1103/PhysRevB.106.115430 for a derivation of the stopping and image forces and for additional results/discussion.

[82] R. Saito, G. Dresselhaus, and M. Dresselhaus, *Physical Properties of Carbon Nanotubes* (Imperial College Press, London, 1998).

[83] P. Giannozzi, S. Baroni, N. Bonini, M. Calandra, R. Car, C. Cavazzoni, D. Ceresoli, G. L. Chiarotti, M. Cococcioni, I. Dabo *et al.*, J. Phys.: Condens. Matter **21**, 395502 (2009).

[84] N. Troullier and J. L. Martins, Phys. Rev. B **43**, 1993 (1991).

[85] J. P. Perdew and A. Zunger, Phys. Rev. B **23**, 5048 (1981).

[86] H. J. Monkhorst and J. D. Pack, Phys. Rev. B **13**, 5188 (1976).

[87] B. Wunsch, T. Stauber, F. Sols, and F. Guinea, New J. Phys. **8**, 318 (2006).

[88] E. H. Hwang and S. Das Sarma, Phys. Rev. B **75**, 205418 (2007).

[89] B. G. Frederick, G. Apai, and T. N. Rhodin, Phys. Rev. B **44**, 1880 (1991).

[90] Z. Y. Ong and M. V. Fischetti, Phys. Rev. B **86**, 165422 (2012).

[91] M. R. Preciado Rivas, M. Moshayedi, and Z. L. Mišković, J. Appl. Phys. **130**, 173103 (2021).

[92] M. N. Gjerding, L. S. R. Cavalcante, A. Chaves, and K. S. Thygesen, J. Phys. Chem. C **124**, 11609 (2020).

[93] K. Akbari, Z. L. Mišković, S. Segui, J. L. Gervasoni, and N. R. Arista, Nanotechnology **29**, 225201 (2018).

[94] V. Andreeva, D. A. Bandurin, M. Luskin, and D. Margetis, Phys. Rev. B **102**, 205411 (2020).

[95] E. Nikulin, D. Mylnikov, D. Bandurin, and D. Svintsov, Phys. Rev. B **103**, 085306 (2021).

[96] A. Politano, Phys. Chem. Chem. Phys. **23**, 26061 (2021).

[97] A. Kononov and A. Schleife, Nano Lett. **21**, 4816 (2021).